

1 **Biomass Estimation from Simulated GEDI, ICESat-2 and NISAR Across Environmental**  
2 **Gradients in Sonoma County, California**

3

4 Duncanson, L.<sup>1,2</sup>, Neuenschwander, A.<sup>3</sup>, Hancock, S.<sup>1,4</sup>, Thomas, N.<sup>2,5</sup>, Fatoyinbo, L.<sup>2</sup>, Simard,  
5 M.<sup>6</sup>, Silva, C.<sup>1</sup>, Armston, J.<sup>1</sup>, Luthcke, S.<sup>7</sup>, Hofton, M.<sup>1</sup>, Kellner, J.<sup>8,9</sup>, Dubayah, R.<sup>1</sup>

- 6 1. Department of Geographical Sciences, University of Maryland, College Park  
7 2. Biospheric Sciences Lab, NASA Goddard Space Flight Center  
8 3. Applied Research Laboratories, University of Texas at Austin  
9 4. School of GeoSciences, University of Edinburgh  
10 5. Earth System Science Interdisciplinary Center, University of Maryland, College Park  
11 6. Radar Science and Engineering Section, NASA Jet Propulsion Laboratory  
12 7. Geodesy and Geophysics Lab, NASA Goddard Space Flight Center  
13 8. Department of Ecology and Evolutionary Biology, Brown University  
14 9. Institute at Brown for Environment and Society, Brown University

15

16 Corresponding author: Laura Duncanson, 2181 Lefrak Hall, University of Maryland, College  
17 Park, Maryland, USA. [lduncans@umd.edu](mailto:lduncans@umd.edu)

18

19 **1.0 Abstract**

20 Estimates of the magnitude and distribution of aboveground carbon in Earth’s forests remain  
21 uncertain, yet knowledge of forest carbon content at a global scale is critical for forest management  
22 in support of climate mitigation. In light of this knowledge gap, several upcoming spaceborne  
23 missions aim to map forest aboveground biomass, and many new biomass products are expected

24 from these datasets. As these new missions host different technologies, each with relative strengths  
25 and weaknesses for biomass retrieval, as well as different spatial resolutions, consistently  
26 comparing or combining biomass estimates from these new datasets will be challenging. This  
27 paper presents a demonstration of an inter-comparison of biomass estimates from simulations of  
28 three NASA missions (GEDI, ICESat-2 and NISAR) over Sonoma county in California, USA. We  
29 use a high resolution, locally calibrated airborne lidar map as our reference dataset, and emphasize  
30 the importance of considering uncertainties in both reference maps and spaceborne estimates when  
31 conducting biomass product validation. GEDI and ICESat-2 were simulated from airborne lidar  
32 point clouds, while UAVSAR's L-band backscatter was used as a proxy for NISAR. To estimate  
33 biomass for the lidar missions we used GEDI's footprint-level biomass algorithms, and also  
34 adapted these for application to ICESat-2. For UAVSAR, we developed a locally trained biomass  
35 model, calibrated against the ALS reference map. Each mission simulation was evaluated in  
36 comparison to the local reference map at its native product resolution (25 m, 100m transect, and 1  
37 ha) yielding RMSEs of 57%, 75%, and 89% for GEDI, NISAR, and ICESat-2 respectively. RMSE  
38 values increased for GEDI's power beam during simulated daytime conditions (64%), coverage  
39 beam during nighttime conditions (72%), and coverage beam daytime conditions (87%). We also  
40 test the application of GEDI's biomass modeling framework for estimation of biomass from  
41 ICESat-2, and find that ICESat-2 yields reasonable biomass estimates, particularly in relatively  
42 short, open canopies. Results suggest that while all three missions will produce datasets useful for  
43 biomass mapping, tall, dense canopies such as those found in Sonoma County present the greatest  
44 challenges for all three missions, while steep slopes also prove challenging for single-date SAR-  
45 based biomass retrieval. Our methods provide guidance for the inter-comparison and validation of  
46 spaceborne biomass estimates through the use of airborne lidar reference maps, and could be

47 repeated with on-orbit estimates in any area with high quality field plot and ALS data. These  
48 methods allow for regional interpretations and filtering of multi-mission biomass estimates toward  
49 improved wall-to-wall biomass maps through data fusion.

50

51 **Keywords:**

52 GEDI, NISAR, ICESat-2, biomass estimation, biomass errors, data fusion

53

54 **2.0 Introduction**

55 **2.1 Background on Biomass modeling/mapping**

56 The accurate estimation of terrestrial forest biomass is crucial for understanding the role of forests  
57 in the global carbon cycle. The total forest carbon reservoir (including below ground carbon) is  
58 equivalent to about 85% of terrestrial stocks and 75% of terrestrial gross primary production (Pan  
59 et al., 2013), yet estimates of the distribution and flux of carbon in Earth's forests remain highly  
60 uncertain, with current global biomass and vegetation structure estimates being too coarse for  
61 many science and policy applications (Hall et al., 2011; Houghton et al., 2012). Further, estimates  
62 of carbon emissions from land use change associated with forest conversion result in large  
63 mismatches between mean global carbon uptake and atmospheric CO<sub>2</sub> growth rates of up to 10 Pg  
64 C year<sup>-1</sup> (Zscheischler et al., 2017) depending on whether the land sink estimation is bottom-up,  
65 i.e. based on long term, ground data (Pan et al., 2013, 2011) or top-down, meaning that it is the  
66 residual of the increase in atmospheric carbon and the net ocean carbon flux (Le Quéré et al.,  
67 2017).

68

69 Remote sensing-based biomass estimates are key to improving bottom-up carbon flux estimates,  
70 as these incorporate both changes in forest extent and biomass density. Similarly, the  
71 implementation of national greenhouse gas (GHG) emission inventories and Payment for  
72 Ecosystem services (PES) schemes such as REDD+ depends on the development of Monitoring,  
73 Reporting, Verification (MRV) guidelines that are based on knowledge of the extent, carbon  
74 density and change of forested areas. The anticipation of PES through REDD+, and the need to  
75 reduce the uncertainties around the global land sink, have resulted in an increased number of  
76 studies on the spatial distribution of aboveground biomass and carbon stocks in forest ecosystems,  
77 such as from global pantropical biomass maps (Baccini et al., 2012; Saatchi et al., 2011).

78  
79 A new generation of active remote sensing technologies will largely fill the need for new global  
80 estimates of aboveground biomass. This paper focuses on three new missions, NASA's Global  
81 Ecosystem Dynamics Investigation (GEDI), NASA's Ice Cloud and land Elevation Satellite  
82 (ICESat-2), and NASA-Indian Space Research Organization (ISRO) Synthetic Aperture Radar  
83 (NISAR). We simulate these three mission datasets with the aim of demonstrating methods for  
84 biomass estimate intercomparison from three different data streams each with its own strengths  
85 and limitations for forest structure mapping.

86  
87 While each of these three missions (NISAR, GEDI and ICESat-2) will make forest canopy  
88 observations that may be used to estimate vegetation biomass, the signals returned from vegetated  
89 surfaces will be influenced by topography and forest structure. The missions with vegetation  
90 structure requirements (GEDI and NISAR) have carefully evaluated these issues in a variety of  
91 landscapes, both from theoretical and applied perspectives (NISAR handbook, Dubayah et al., in

92 review). The impacts of surface structural complexity for ICESat-2, conversely, are relatively  
93 unknown in temperate systems given the lack of a vegetation product requirement by the ICESat-  
94 2 mission. Scientists on each mission team have predicted the expected performance of the  
95 missions for biomass (Neuenschwander and Magruder, 2016; Yu and Saatchi, 2016, GEDI  
96 ATBDs), but no assessment has been conducted exploring potential utility at a single site for all  
97 three missions. Fusing SAR and lidar datasets over forested areas and developing new algorithms  
98 that incorporate the benefits of each dataset may improve our ability to estimate forest biomass  
99 with higher accuracies and at spatial resolutions appropriate for land management.

100

101 A consistent exploration of the biomass estimation limitations of these upcoming datasets will help  
102 inform the development of fusion techniques, particularly in structurally complex environments  
103 (e.g. high biomass mixed forests in mountainous areas). It is well accepted that errors increase  
104 with increasing biomass densities, both due to a) increased natural structural variability in mature,  
105 higher biomass forests systems, b) increased edge effects, particularly in areas with wider tree  
106 crowns, and c) increased errors associated with the application of allometric models (Réjou-  
107 Méchain et al., 2019). Therefore a deviation in, say, a GEDI biomass estimate from a reference  
108 pixel biomass estimate in a mature, high biomass area may well be within the wider confidence  
109 limits of the reference map in that area as compared to a tighter confidence interval in a lower  
110 biomass forest. Thus, all airborne lidar reference maps have limitations in their utility as reference  
111 datasets.

112

113 The goals of this study are three-fold. First, to demonstrate methods for validation of satellite-  
114 based biomass estimates through comparison to a locally calibrated airborne lidar biomass map.

115 Second, to determine trends in relationships between biomass estimation error and environment  
116 for GEDI, ICESat-2 and NISAR in a particularly challenging high biomass domain, and third, to  
117 test the application of GEDI's biomass algorithms on ICESat-2 data.

118

## 119 **2.2 SAR and Lidar Mission Status**

### 120 **2.2.1 GEDI**

121 The GEDI mission is the first spaceborne lidar designed specifically to study forest structure  
122 (Dubayah et al., under review). GEDI is a NASA Earth Venture Instrument (EVI) that was selected  
123 in 2014, and implements a 3-laser, full waveform recording Lidar instrument operating from the  
124 Japanese Experimental Module's Exposed Facility (JEM-EF) on the International Space Station  
125 (ISS). GEDI launched on December 5, 2018, and will operate for a nominal 2-year minimum  
126 period, producing ~10 billion cloud-free land surface observations. GEDI's 3 lasers operate at  
127 1064 nm, while one laser is split into two weaker energy beams, resulting in four GEDI beams,  
128 each illuminating footprints (areas on the Earth's surface from which Lidar energy is reflected)  
129 with a ~25 m diameter. These beams are optically dithered to produce eight ground tracks with  
130 approximately 60 m along track sampling returning full waveform lidar observations with a 2-3  
131 cm vertical measurement accuracy. GEDI full waveform along track observations are acquired  
132 from 8 tracks spaced 600 m apart effectively sampling data from a 4.2 km wide swath. The GEDI  
133 instrument has the ability to point or roll about an axis approximately aligned with the ISS velocity  
134 vector. Therefore, the instrument pointing enables optimal sampling such that the center of the  
135 GEDI swath follows a set of pre-defined Reference Ground Tracks (RGTs) even though the ISS  
136 is not in a repeating orbit. The RGTs are computed to be as congruent with the ISS orbit as

137 possible, facilitating minimal instrument off-pointing, therefore at the same 51.6 degree inclination  
138 as the ISS orbit.

139

140 For each footprint, GEDI will have a suite of waveform metrics, including canopy height and  
141 relative height (RH) metrics, canopy profile metrics, and ground elevation. These waveform  
142 metrics are also used to estimate aboveground biomass density (AGBD) using empirically derived  
143 calibration models. GEDI footprint-level biomass estimates will then be gridded to 1 km products,  
144 although as aforementioned GEDI's gridding algorithm is not assessed in this paper. The GEDI  
145 Science Definition Team (SDT) has compiled a global database of coincident *in situ* field and  
146 airborne lidar datasets to develop the footprint-level calibration models which will convert GEDI  
147 metrics to biomass. In this process, airborne lidar data are used to simulate GEDI waveforms  
148 (Hancock et al., 2019), and these waveforms are used to train the biomass calibration models that  
149 are applied to the on-orbit GEDI data. For a detailed overview of the generation of GEDI's  
150 footprint level biomass model, please refer to (GEDI User Handbook)

151

### 152 **2.2.2 NISAR**

153 NISAR is a multi-disciplinary mission born from a joint partnership between the National  
154 Aeronautics and Space Administration (NASA) and Indian Space Research Organization (ISRO),  
155 and its platform will host both L-band (24 cm wavelength) and S-band (10 cm wavelength) radars.  
156 NISAR will collect data with a spatial resolution of 7m over a swath width ~242 km using a 12 m  
157 diameter deployable mesh reflector (NISAR User Handbook). NISAR is scheduled to launch at  
158 the end of 2021 for a minimum 3-year mission with capacity for extended operations. The satellite  
159 will be in a 12-day repeat orbit at an altitude of 740 km (Rosen et al., 2016). The mission will

160 therefore achieve global coverage every 6 days considering both ascending and descending orbital  
161 passes. The current mission plan is for co-polarization mode (HH) acquisitions every 6-days, and  
162 cross-polarization mode (HV) acquisitions three times every 24 days. This results in each location  
163 on Earth being imaged ~60 times each year.

164

165 The NISAR L-band radar backscatter measurements will enable the generation of an annual global  
166 biomass map with a spatial scale of 1 ha. The mission is required to cover at least 80% of forested  
167 areas with biomass  $\leq 100$  Mg/ha and with no more than 20% error. Forest disturbance and recovery  
168 will also be monitored annually at the 1 ha resolution (Yu and Saatchi, 2016). The radar  
169 measurements will provide these biomass estimates irrespective of illumination and atmospheric  
170 conditions and will not be perturbed by cloud cover which is prominent in the tropics.

171

### 172 **2.2.3. ICESat-2**

173 The ICESat-2 satellite was launched on September 15, 2018, and provides a global distribution of  
174 geodetic measurements from a space-based laser altimeter of both the ground and canopy surfaces.  
175 The primary science objective of these measurements over land is the estimation of vegetation  
176 canopy height which will also enable height-based biomass estimation. The Advanced  
177 Topographic Laser Altimeter System (ATLAS) instrument on-board ICESat-2 is a photon  
178 counting laser altimeter. ICESat-2 will generate two geophysical data products specifically  
179 focused on land and vegetation: ATL08, the Level 3 along-track data product and ATL18, the  
180 Level 4 gridded product. ATL08 will report terrain height estimates, canopy height estimates, and  
181 relative height metrics such as: RH25, RH50, RH60, RH70, RH75, RH80, RH85, RH90, and RH98  
182 at a 100 m step.

183

184 ATLAS operates at 532 nm in the green range of the electromagnetic (EM) spectrum and fires at

185 a rate of 10 kHz. The combination of the laser repetition rate and satellite velocity will result in

186 one outgoing laser pulse approximately every 70 cm on the Earth’s surface and each spot on the

187 surface is ~13 m in diameter (Magruder et al., 2020). Over vegetation, the number of detected,

188 returned photons from each outgoing laser pulse is expected to range between 0 to 4 photons,

189 depending upon canopy cover, atmospheric transmission, and surface reflectance

190 (Neuenschwander and Pitts, 2019). That detection can occur anywhere within the vertical

191 distribution of the reflected signal, that is, anywhere within the vertical distribution of the canopy.

192 This uncertainty of where the photon will be returned is referred to as the vertical sampling error

193 (Neuenschwander and Magruder, 2016). The photon-counting technology has many advantages

194 for space-based altimetry but also has challenges, particularly with delineating signal from

195 background noise. Simulation studies to estimate vertical sampling error indicate that the canopy

196 heights reported on the ATL08 data product will underestimate the top canopy height in the range

197 of 1 – 4 m at its 100-m transect resolution (Neuenschwander and Magruder, 2016). Due to the high

198 laser pulse repetition rate and smaller footprint size, the along-track point density is relatively high

199 and the ICESat-2 algorithms have been written to separate vegetation returns from ground returns,

200 even in areas of high relief – an improvement from ICESat/GLAS where the topographic signal

201 was convolved with the vegetation signal in areas with relief greater than 10% (Chen, 2010;

202 Duncanson et al., 2010; Hilbert and Schmallius, 2012; Neuenschwander and Pitts, 2019).

203 Table 1 Summary of key mission specifications and resolutions

	<b>ICESat-2</b>	<b>GEDI</b>	<b>NISAR</b>
Launch Date	September 15, 2018	December 5, 2018	2022
Wavelength	532 nm (green)	1064 nm (near IR)	S&L band

Geographic Coverage	Global	ISS: +/- ~ 51.6°	Global
Measurement Strategy	6 tracks from 1 laser (3 power tracks)	8 tracks from 3 lasers (4 power tracks, 4 coverage tracks)	Wall-to-wall
Native Measurement Resolution	~13 m footprints returning 0-4 photons	~25 m footprints returning full waveforms	3 m x 8 m slant range resolution
Biomass Product Resolution(s)	NA	25 m footprint estimates; 1 km gridded estimates	1 ha
Resolution Tested in this Study	100 m along track transects	25 m circular footprint	1 ha

204

#### 205 **2.2.4. Mission Biomass Requirements**

206 The GEDI and NISAR missions both have formal requirements for generating data to enable the  
207 production of biomass maps, while ICESat-2 has no formal biomass requirement. GEDI's science  
208 requirements are to measure forest height and vertical structure at the footprint (~25m) resolution,  
209 and to estimate biomass at the specified grid resolution of 1 km with an uncertainty of 20%  
210 Standard Error (SE) or better in 80% of the GEDI domain 1 km cells. The NISAR mission is  
211 required to enable estimates of biomass annually with a spatial resolution of 1 ha, with an accuracy  
212 of 20Mg/ha (RMSE) in at least 80% of forest areas with biomass below 100 Mg/ha. GEDI and  
213 ICESat-2, as sampling missions, will have gaps across tracks, and also from clouds, while NISAR  
214 will provide wall-to-wall data. GEDI is designed to provide data for measuring forest structure  
215 across all ranges of biomass up to ~ 99.8% canopy cover, while NISAR's requirements are limited  
216 to biomass values below 100 Mg/ha (up to ~70% canopy cover in Sonoma County). ICESat-2 is  
217 expected to provide estimates for a range of biomass between GEDI and NISAR, limited mainly  
218 by its ability to penetrate canopy cover, although this limit has not yet been established. Because  
219 of the ISS orbit, GEDI will only collect data under the ISS orbit, between 51.6° North and South,  
220 while both ICESat-2 and NISAR provide global coverage. Native footprint sizes are about 25 m

221 for GEDI and 3 m x 8 m slant range resolution for NISAR. ICESat-2 collects approximately 0-4  
222 photons from each ~13 m footprint over vegetated surfaces, but densely overlapping footprints  
223 (spaced 70 cm along track) provide canopy height transects with a length of about 100 m and width  
224 of ~13 m. Thus, in this paper we focus on estimating biomass not at the expected mission gridded  
225 product resolutions, but at the resolution of the finest biomass estimates expected from each  
226 mission (i.e. 25 m diameter circles for GEDI, 100 m transects for ICESat-2, and in this case an  
227 aggregated 1ha resolution for NISAR, although the measurement units for NISAR are higher  
228 resolution). Table 1 provides a summary of the three missions addressed in this study, including  
229 the expected gridded mission biomass products in comparison to the scale at which we conduct  
230 our analyses using simulated mission datasets.

231

### 232 **3.0 Methods**

233 This study presents a comparison of biomass estimates from simulated spaceborne datasets to a  
234 local reference biomass map, and calculates multiple statistics for each spaceborne estimate. To  
235 help guide the reader in the interpretation of our results, for the remainder of the paper we use the  
236 following definitions: Uncertainty is defined as the 90<sup>th</sup> percentile confidence interval around a  
237 prediction of aboveground biomass density, both for reference pixels and simulated spaceborne  
238 estimates. In this paper we define error as the deviation between a biomass estimate and its true  
239 value, which again we assume here to be its airborne lidar reference value. A more accurate  
240 estimate will have a lower deviation between the estimate and the reference value. The Root Mean  
241 Squared Error (RMSE) then is defined as the square root of the mean of the squared deviations  
242 between simulated spaceborne pixel estimates and airborne lidar reference map estimates. We  
243 concede that this is technically incorrect, as residuals by definition are deviations between

244 estimates and observations, but observations of forest AGBD are not available in the vast majority  
245 of field or lidar studies, and typically rely on the application of allometric models as we have done  
246 here (Clark and Kellner, 2012).

247

### 248 **3.1. Study Area**

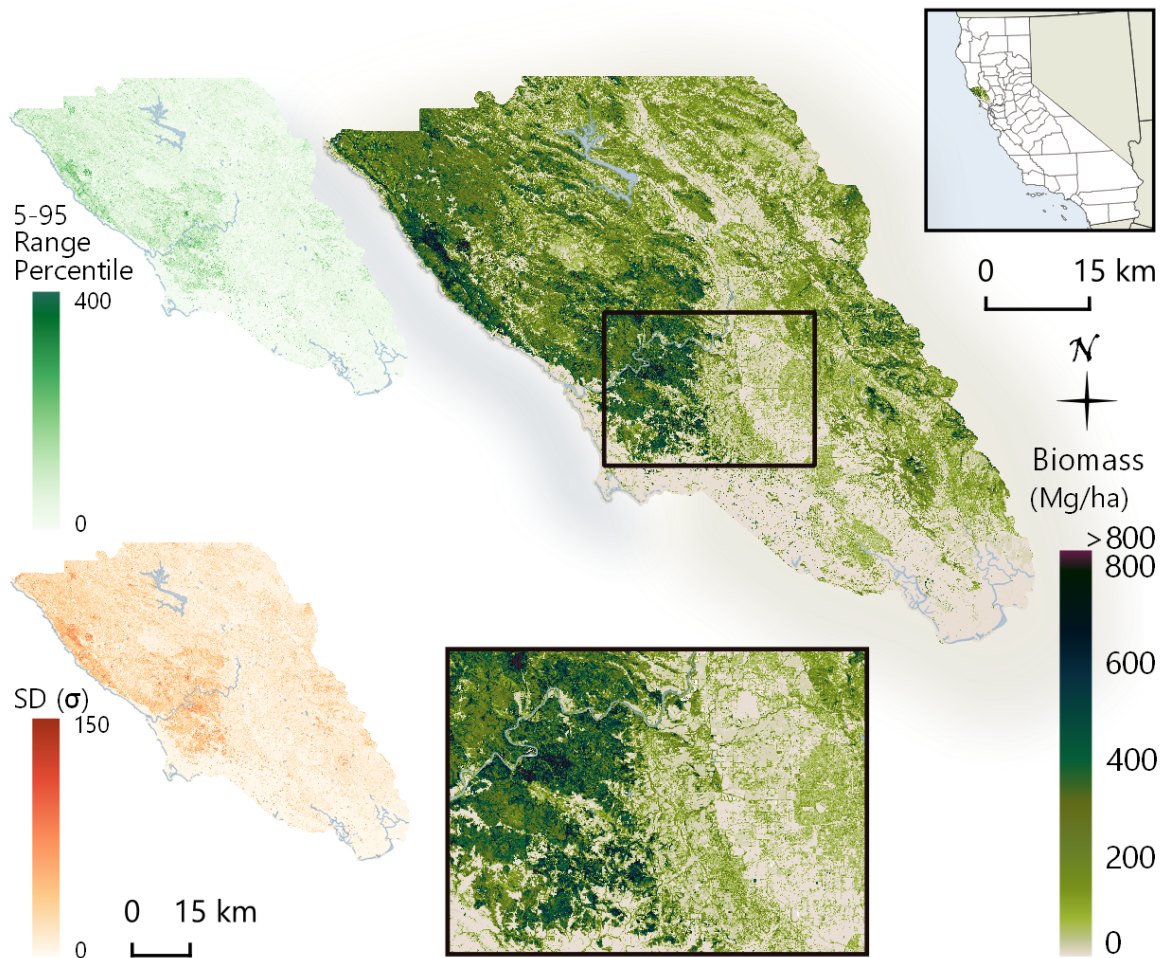
249 This study was conducted in Sonoma County, California, where airborne proxies for all three  
250 missions (GEDI, NISAR and ICESat-2) are available. The majority of Sonoma County is classified  
251 as either conifer forest, grassland, or shrubland, with large portions of developed areas, mixed  
252 forests, and cropland (Homer et al., 2015). In terms of biomass composition, more than half of the  
253 modeled biomass in Sonoma County falls in pixels classified as conifer forests, followed by  
254 scrubland and mixed forest. Fig 2 shows the distribution of biomass, percent canopy cover, slope,  
255 and forest height across the study area. The study area spans wide variety of elevation, slope, tree  
256 height, canopy cover and biomass, thus enabling an analysis of anticipated mission data strengths  
257 and limitations in different forest conditions.

### 258 **3.2 Data**

#### 259 **Sonoma ALS and Biomass Map**

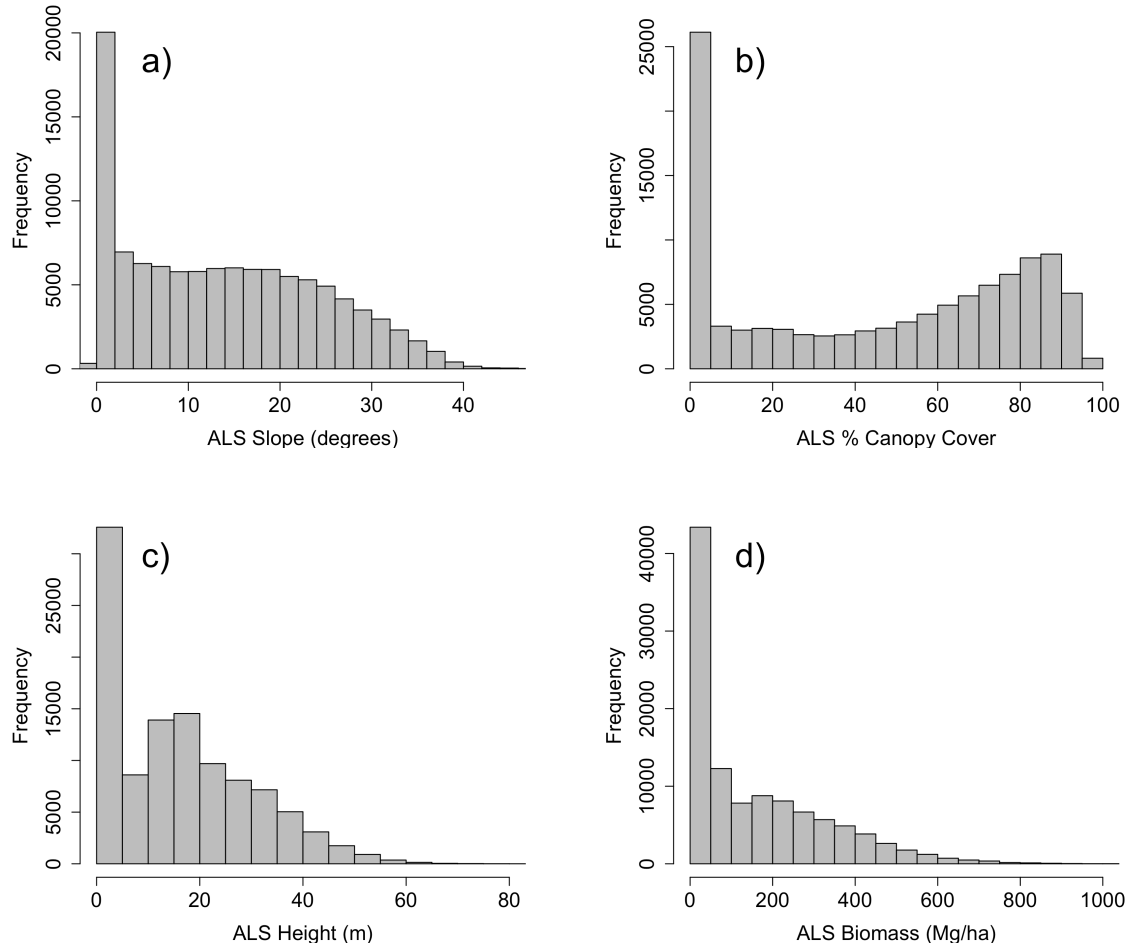
260 Wall-to-wall ALS were collected over Sonoma County in the fall of 2013 using Leica ALS50 and  
261 ALS70 instruments giving coverage over the whole county at 14 points m<sup>-2</sup> (Dubayah et al., 2013).  
262 These data were used to generate a 30 m biomass map for all of Sonoma County (Dubayah et al.,  
263 2013) using a random forest model and calibrated with 166 field plots collected at a random sample  
264 of locations stratified by land cover type (Duncanson et al., 2017; Huang et al., 2017). These field  
265 plots largely missed the highest biomass areas of Sonoma County, and the maximum biomass  
266 density was ~500 Mg/ha, thus the random forest model set all high biomass redwood forests to

267 this maximum value. A new reference map was regenerated, using 30 additional plots sampled in  
268 redwood forests across the county using an Ordinary Least Squares (OLS) modeling approach (SI  
269 Fig 1), and the variance covariance matrix from this model was sampled to produce 1000 estimates  
270 for every 30 m pixel across Sonoma County. 90<sup>th</sup> percentile confidence intervals were calculated  
271 from the 1000 sets of predicted biomass for each pixel, and as expected we find wider confidence  
272 intervals in higher biomass forests (Fig 1). Developed areas were masked from this analysis using  
273 a high resolution forest non-forest mask described in (Dubayah et al., 2013).  
274

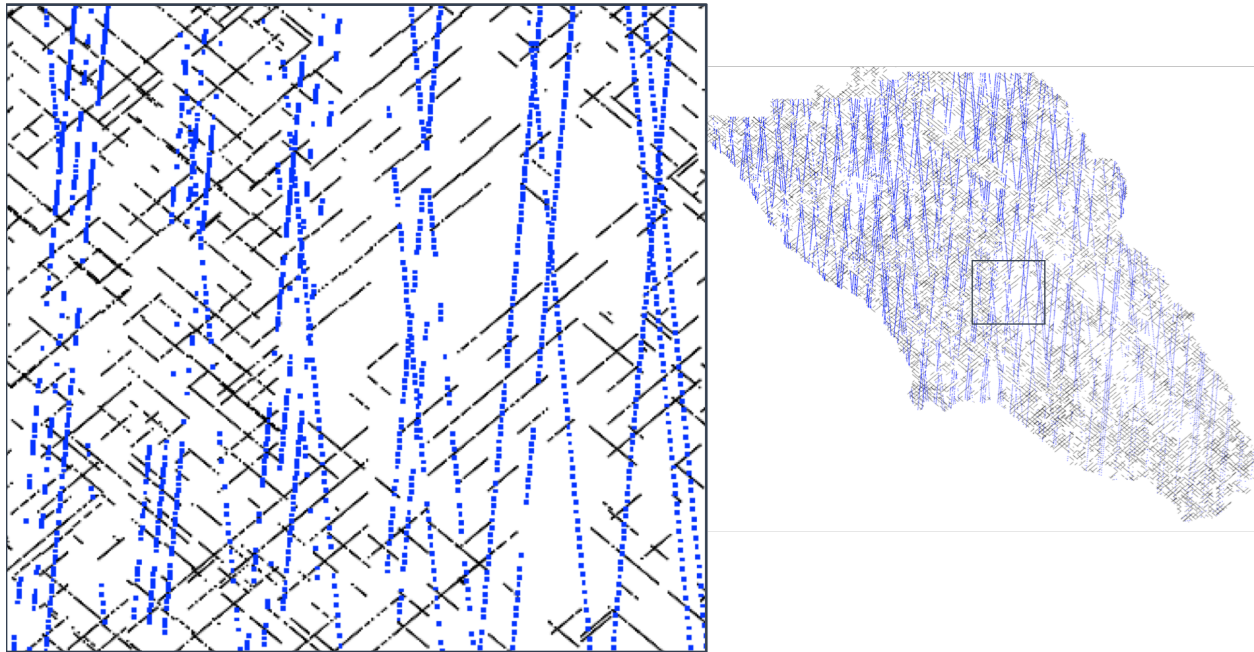


275

276 **Fig 1 A Sonoma County-wide 30 m ALS biomass map was used as the biomass reference**  
277 **map for this study. The 90<sup>th</sup> percentile and standard deviations of biomass from a model**  
278 **bootstrapping are shown on the left.**



279  
280 **Fig 2 Histograms of ALS-derived (a) slope, (b) % canopy cover (b), (c) height and (d)**  
281 **biomass from the 30 m ALS data across the study area.**



282

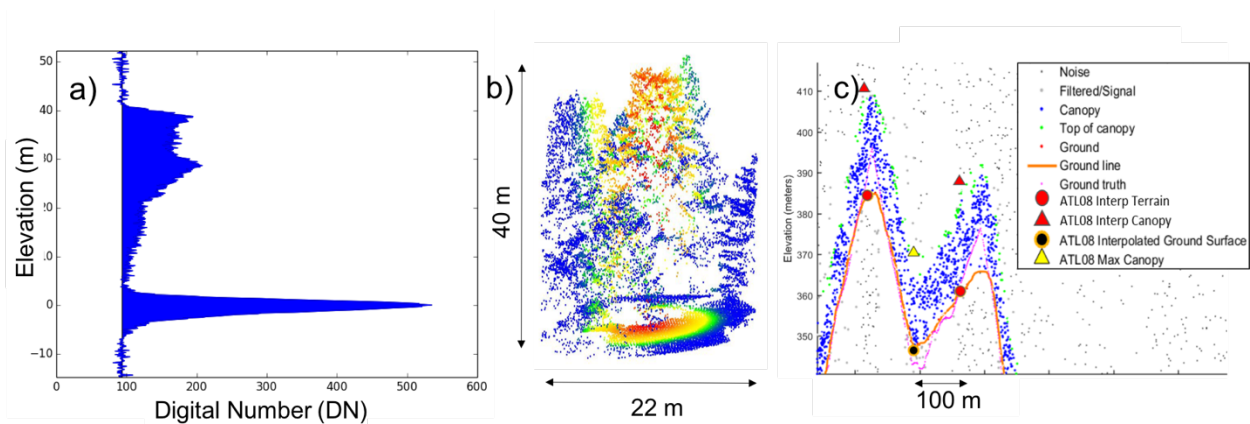
283 **Fig 3. UAVSAR data were acquired over the majority of the county in 2014, serving as a**  
284 **proxy for NISAR, while lidar mission simulations were generated representing two years of**  
285 **on-orbit acquisitions for both GEDI (black) and ICESat-2 (blue).**

286

### 287 **GEDI simulations**

288 ALS data were processed to simulate GEDI waveforms across the entire county representing two  
289 years of on-orbit performance (Fig 3). The GEDI simulator is described in detail and validated in  
290 Hancock et al., (2019). Waveforms are simulated following the methods proposed in (Blair and  
291 Hofton, 1999), and white Gaussian noise is added (Hancock et al., 2011) to provide the same  
292 signal-to-noise ratio (SNR) predicted by pre-launch analysis of the instrument performance for  
293 mean atmospheric transmission, solar background illumination and the expected detector response  
294 (Davidson and Sun, 1988). This allows GEDI-like signals to be generated from any ALS data,  
295 with simulations having the same properties and expected measurement errors as GEDI. GEDI's  
296 SNR is related to beam sensitivity, i.e. the percentage of canopy cover through which we expect

297 to be able to detect the ground 90% of the time. GEDI's power beams are expected to return a  
 298 reliable ground signal beneath 99.5% canopy cover at night, and 94% canopy cover during the  
 299 day, assuming 80% atmospheric transmittance with a 3db margin loss over design estimates. These  
 300 increase to 97% during the day and 99.75% during the night if the 3 dB margins are maintained.  
 301 Under the same conditions, the coverage beam is to produce reliable ground returns under 96%  
 302 canopy cover by night and 92% canopy cover by day , increasing to 98 and 96% with preserved  
 303 margins (Hancock et al., 2019).



304  
 305 **Fig 4: Simulated GEDI waveforms (a) are vertical aggregations of point clouds (b) in GEDI**  
 306 **sized footprints, which have been modeled to match expected pulse shape and spatial**  
 307 **distribution of reflected energy for GEDI. ICESat-2 simulations (c) use degraded point**  
 308 **clouds along transects with added background noise. Simulated photon returns are**  
 309 **classified as noise, ground, or vegetation returns (c).**

310  
 311 From the simulated waveforms (Fig 4a), the ground elevation is estimated and Relative Height  
 312 (RH) metrics are extracted, which are related to biomass (Drake et al., 2002). The accuracy of  
 313 these RH metrics depends on the accuracy of the ground elevation estimation for each waveform.  
 314 While the GEDI mission's ground finding algorithm is still under development, for this study we

315 used the ground finding algorithm in libClidar (Hancock et al 2017), with denoising parameters  
316 tuned for Sonoma County. A two-year simulation of GEDI's track sampling was conducted at a  
317 global scale as part of GEDI's pre-launch mission science analysis. The sampling simulation used  
318 two-years of ISS orbits in combination with an optimized pointing algorithm to define and acquire  
319 the GEDI RGTs. These simulated orbital tracks are combined with an assumption of 50% cloud  
320 cover and filtering leaf-off data, to generate distributions of GEDI observations over the study site  
321 (Fig 3). GEDI metrics were extracted for biomass estimation using four noise cases representing  
322 realistic combinations of GEDI's power and coverage beams and day and night acquisitions.

323

#### 324 **ICESat-2 Simulations**

325 The uncertainty in the ATL08 canopy height is influenced by both the vertical sampling error as  
326 well as the solar background noise, which will impact the terrain and canopy height retrievals by  
327 the ATL08 algorithm. To simulate ICESat-2 data, the high density ( $\sim 14$  points  $m^{-2}$ ) ALS data were  
328 sampled along five ICESat-2 ground tracks as described in Neuenschwander and Magruder (2016).  
329 The ICESat-2 frozen repeat orbit and its associated RGTs were developed as part of the mission  
330 definition and analysis. The ground tracks used in the study are those from the mission simulation  
331 and include the planned satellite off-pointing for vegetation sampling. Within each 13 m diameter  
332 simulated ICESat-2 footprint, the vertical distribution of the airborne data was taken as  
333 representative of the probability of a photon returning from a given elevation. This distribution  
334 was used to weight the random sample the "photons". The number of photons sampled for each  
335 outgoing ICESat-2 shot is based on a random selection from a Poisson distribution for the expected  
336 number of returned photons given a specific surface type. We simulate two different cases, one  
337 with an average of one photon returned per shot, and a second with an average of two photons

338 returned per shot. Based on actual on-orbit data from ICESat-2, the average photon rate for 18  
339 granules over Sonoma County is found to be 1.57 photons per shot with a minimum value of 0.98  
340 photons per shot and a maximum value of 2.06 photons per shot. Thus, the data low and high  
341 photon rates utilized for the simulations in this study nicely book-end the expected performance  
342 for ICESat-2 in this region. In addition to the simulated ICESat-2 photons, canopy height metrics  
343 (RH25, RH50, RH60, RH75, RH90, RH95, and RH100) were calculated from the ALS data within  
344 each footprint for comparison. Noise was added to the sampled “photons” from the airborne lidar  
345 data to simulate various solar background conditions. The simulated dataset produces a geolocated  
346 point cloud similar to that from the ICESat-2/ATLAS measurements (ATL03) which subsequently  
347 serves as the input to the ATL08 (Land/Veg) terrain and canopy height retrieval algorithm  
348 (Neuenschwander and Pitts, 2019).

349

350 The ATL08 algorithm works by first isolating the signal photons from the noise photons in the  
351 geolocated point cloud (ATL03). Once the signal photons are identified, a ground surface and a  
352 top of canopy surface are estimated using a series of iterative filters. After the surfaces are defined,  
353 the individual photons are attributed as being reflected from the terrain or canopy based on a  
354 threshold which is a dynamic point spread function that is dependent upon the sensor uncertainty  
355 as well as geolocation and topographic uncertainty. The dynamic point spread function can vary  
356 from 50 cm to 1 m. Once the photons are attributed as either terrain, canopy, or top of canopy,  
357 they are used to calculate statistics within a 100 m step size along the ground track. For example,  
358 every 100 m, ATL08 will report statistics such as mean terrain height or standard deviation of  
359 terrain height based on the photons attributed as terrain within a 100 m step. The derivation of  
360 canopy height on the ATL08 data product is defined as the 95 percentile height of the photons

361 attributed as canopy, where the height of each photon is calculated with respect to the terrain  
362 elevation interpolated directly beneath the photon. The RH metrics are thus calculated as the  
363 relative height of the cumulative distribution for all canopy photons, similar to how airborne lidar  
364 height percentiles are typically calculated. The output of labeled photons from the ATL08  
365 algorithm using simulated ATLAS data over Sonoma County is shown in Fig 4c.

366

### 367 **NISAR Simulations (UAVSAR)**

368 UAVSAR is an operational fully polarimetric L-band (wavelength of 23.5 cm) synthetic aperture  
369 radar (Hensley et al., 2009) designed and operated by NASA's Jet Propulsion Laboratory to  
370 provide robust repeat pass radar interferometric measurements of deformation from both natural  
371 and anthropogenic sources. UAVSAR data were collected over Sonoma County on August 29<sup>th</sup>  
372 2014 with a flight bearing of approximately 55°. Six flights-lines were acquired over Sonoma  
373 county. Each image is 20 km wide and approximately 155 km long, with look angles for all swaths  
374 ranging from the near to far range between 21° to 65°, respectively.

375

376 Complex topography causes increased variation in SAR imagery and limits its use over irregular  
377 terrain unless corrected for. Therefore, the radar imagery was radiometrically corrected for  
378 variations in illuminated area on the ground, as well as variations in forest reflectivity with viewing  
379 and terrain geometry using the radar look angle and range slope, as outlined by (Simard et al.,  
380 2016). The ALS digital elevation model (DEM) was merged with the SRTM DEM to cover the  
381 full extent of the UAVSAR data, and utilized to perform the radiometric correction. HH, HV and  
382 VV polarizations were processed with a native pixel spacing of 0.00005556 degrees (6.14 m at the

383 equator). The radiometric and geometrically corrected UAVSAR imagery was re-projected to  
384 UTM and resampled to 30 m pixels to match the ALS biomass map using bilinear interpolation.

385

### 386 **3.3 Biomass Modeling**

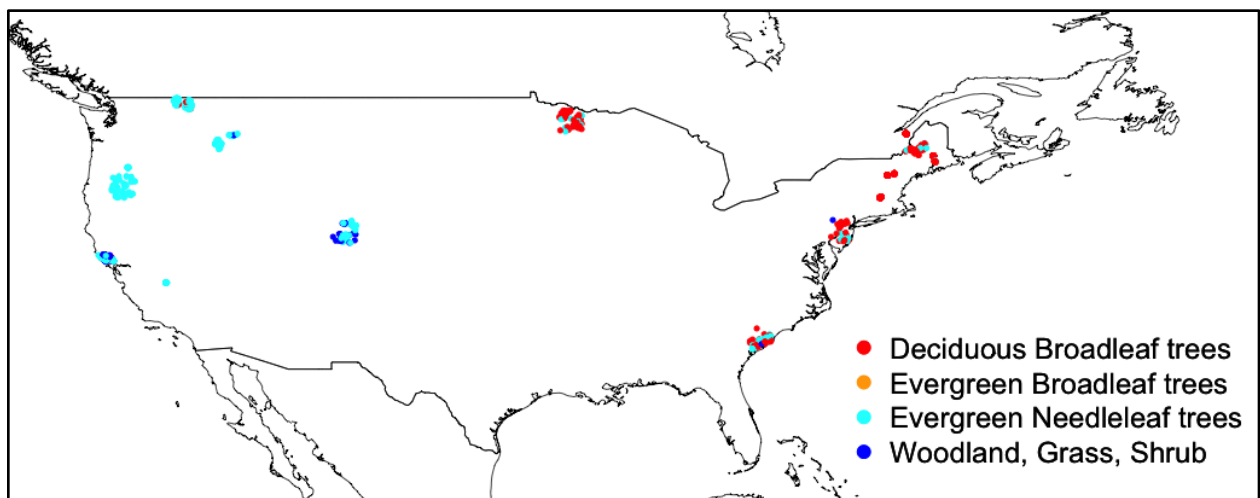
387 GEDI will produce global biomass products as given in GEDI L4A and L4B Algorithm  
388 Theoretical Basis Documents (Patterson et al., 2019) and these algorithms will include calibration  
389 data from a large, geographically distributed set of field sites. GEDI uses existing airborne lidar  
390 and field data and a GEDI waveform simulator to produce a global set of biomass calibration sites  
391 (see Fig 5). The NISAR mission will produce biomass data products up to 100 Mg/ha over a select  
392 number of globally distributed sites that includes airborne and/or spaceborne L-band backscatter  
393 and ALS over a range of ecosystems. In this study, we use GEDI's L4A biomass models for  
394 simulating GEDI biomass estimates, but at the time of publication NISAR's calibration sites are  
395 not finalized, nor are the data available, so the final NISAR algorithms were not available. Instead,  
396 we developed a biomass-backscatter relationship between L-band backscatter and the Sonoma  
397 county-wide ALS biomass map. We compared height metrics from simulated GEDI and ICESat-  
398 2 in an attempt to determine whether GEDI's algorithms can be leveraged to produce ICESat-2  
399 biomass products, and applied versions of the GEDI algorithms that only consider selection of RH  
400 metrics available in the ICESat-2 ATL08 product.

401

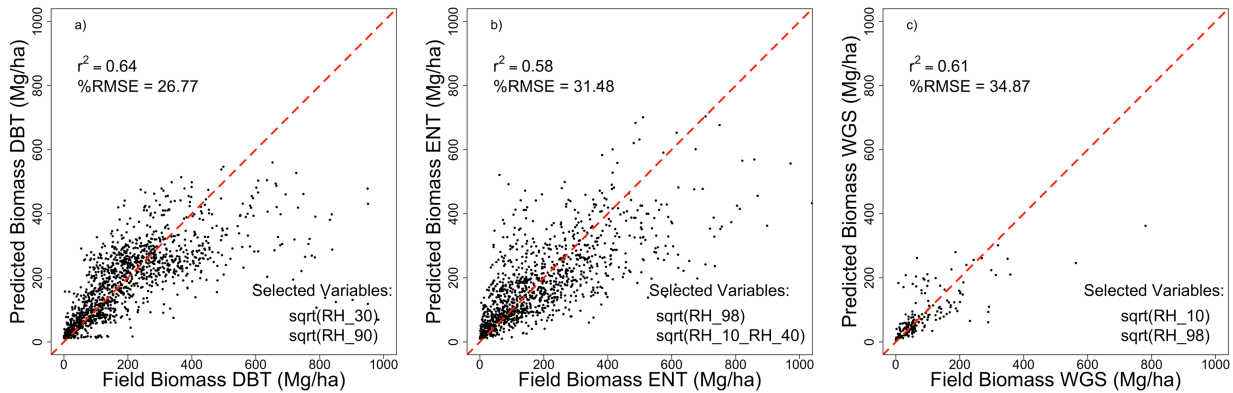
#### 402 **3.3.1 GEDI and ICESat-2 Biomass Models**

403 For its footprint-level biomass algorithms, GEDI stratifies the globe by MODIS estimated Plant  
404 Functional Type (PFT) and region (usually continent). For Sonoma County, three GEDI models  
405 were used; one for prediction in North American Evergreen Needleleaf Trees (ENT), one for North

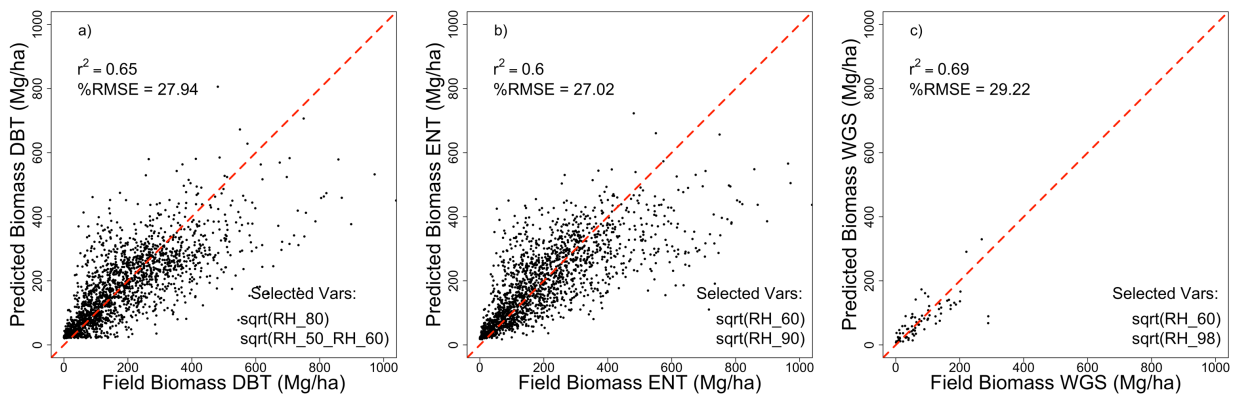
406 American Evergreen Broadleaf Trees (EBT) , and one for North American Woodlands, Grasslands  
407 and Shrublands (WGS) (Fig 6). These models were also re-fit for application to ICESat-2 by only  
408 considering predictors of RH50, RH60, RH70, RH80, RH90, RH98, and their interaction terms  
409 (Fig 7). These models were fit at the nominal GEDI resolution over GEDI-sized field plots with  
410 simulated waveforms from airborne lidar data. These are OLS models fit between square root  
411 transformed AGB and square root transformed RH metrics, with an exhaustive variable selection  
412 algorithm applied that allowed up to four predictors to be selected for each model. As with the  
413 generation of confidence intervals in the airborne reference map, the variance covariance matrices  
414 from these model fits was sampled 1000 times per model, and each iteration was applied to each  
415 simulated GEDI and ICESat-2 data point to produce confidence intervals around GEDI and  
416 ICESat-2 estimates of AGB. Please note that while Sonoma County field plots are included in  
417 GEDI's L4A model fitting, for the purposes of this paper to ensure the application was realistic to  
418 independent datasets, the Sonoma County field and lidar data were removed from GEDI's L4A  
419 database.



422 **Fig 5** The GEDI cal/val database for the United States was used to generate empirical  
 423 **models for both GEDI and ICESAT-2 from linked field plots and ALS datasets. These US-**  
 424 **wide models were applied to the simulated GEDI & ICESAT-2 datasets in Sonoma County**  
 425



426  
 427 **Fig 6** The US-wide GEDI biomass model (applied to simulated GEDI) used an OLS model  
 428 **with exhaustive variable selection for Deciduous Broadleaf Trees (DBT), Evergreen**  
 429 **Needleleaf Trees (ENT) and Woodland Grassland Shrub (WGS). The selected variables are**  
 430 **displayed in the bottom right, and model accuracies are calculated by k-fold cross**  
 431 **validation.**



432  
 433 **Fig 7** The US-wide GEDI biomass models allowing only selection of variables available in  
 434 **the ICESat-2 ATL08 algorithm for Deciduous Broadleaf Trees (DBT), Evergreen**

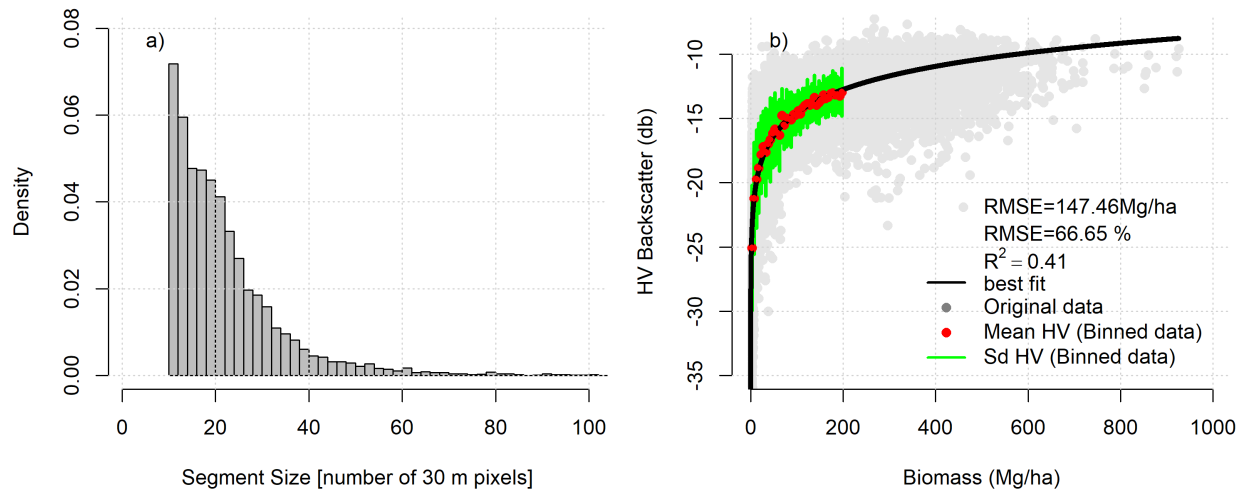
435 **Needleleaf Trees (ENT) and Woodland Grassland Shrub (WGS) These models were**  
436 **applied to simulated ICESat-2 data across the study area.**

437

### 438 **3.3.2 NISAR Biomass Model**

439 Sonoma county presents an ambitious site for UAVSAR (and NISAR) in quantifying values of  
440 biomass which are generally in excess of the NISAR mission requirement, and within a  
441 challenging topographic environment. However, radar imaging provides a spatially continuous  
442 observation of the landscape. As such, it is possible to analyze the imagery following landscape  
443 features and patterns, and determine forest structural attributes on forest patches rather than on  
444 intrinsically square pixels or grid cells. The UAVSAR mosaic was spatially segmented into image  
445 objects using the segmentation algorithm described in Clewley et al., (2014). This utilizes k-means  
446 and iterative elimination to group similar neighboring pixels into objects of a user-defined  
447 minimum size. The UAVSAR mosaic was segmented with a minimum object size of 11 pixels,  
448 creating objects of approximately 1 ha and greater. The objects were populated with the mean HV  
449 backscatter pixel values and converted to decibel (dB). The mean ALS derived biomass, mean  
450 UAVSAR look angle and mean UAVSAR derived slope were also attributed to objects. To this  
451 effect the image objects describe the radiometric and viewing geometry characteristics of the  
452 underlying land-cover type.

453



454

455 **Fig 8 The study area was segmented based on UAVSAR backscatter. A) shows a histogram**  
456 **of the object sizes (number of 30 m pixels). The average HV backscatter per biomass bin was**  
457 **used to generate a backscatter to biomass curve (b). The black solid line is the best fit, and**  
458 **the vertical green lines represent the standard deviation of HV Backscatter in each biomass**  
459 **bin. The gray dots are the average of HV backscatter and biomass data per object.**

460

461 SAR backscatter is known to increase with biomass up to a saturation level for a range of radar  
462 wavelengths (Luckman et al., 1998; Mitchard et al., 2009). The relationship between UAVSAR  
463 HV backscatter and ALS derived biomass was established, using image objects with a mean look  
464 angle between 33° to 47° to simulate the NISAR viewing geometry. With its 36 looks (number of  
465 pixels averaged to reduce speckle noise), UAVSAR closely simulates NISAR annual time-series  
466 with 30 ascending and 15 descending passes. Backscatter was averaged at a 5 Mg/ha biomass  
467 interval (Fig 8b) yielding the relationship:

468

469

$$\text{HV Backscatter (db)} = -26.457 + 2.586 * \log [\text{Biomass (Mg/ha)}]$$

470

471 
$$\text{Biomass (Mg/ha)} = \exp\left(\frac{\text{HV Backscatter (db)} + 26.457}{2.586}\right)$$

472

473 Only objects with a mean biomass  $\leq 200$  Mg/ha and UAVSAR perspective slope  $\leq 10$  degrees were  
474 used to fit the relationship, but it was applied to all objects. We also developed backscatter models  
475 based on the full range of slopes and biomass densities, but a flat, low biomass model produced  
476 lower errors, even in sloped or higher biomass areas. This model was applied to the full area of  
477 UAVSAR coverage in Sonoma, at a minimum 1 ha scale. Residual error was generated by  
478 comparing the predicted UAVSAR biomass with the mean 30 m ALS derived biomass estimate,  
479 per image object.

480

### 481 **3.4 Comparison to Lidar Reference Map**

482 For any spaceborne biomass estimate, validation using reference data is challenging given that  
483 nearly all reference data will include error. This is a challenge across the forest mapping  
484 discipline where field measurements contain uncertainties, but is particularly true of biomass  
485 which is typically estimated through the application of some allometric model e.g. (Chave et al.,  
486 2014). In this study we did not propagate error from field estimates of biomass to the reference  
487 (or spaceborne) estimates, which is consistent with comparable studies (see McRoberts et al.,  
488 2018, for an exception). However, uncertainties in field estimates of biomass are subsumed into  
489 the model fit errors, to the extent the model training data is representative of the variability  
490 driven by field plot biomass (Patterson et al., 2019). For the ALS reference map, the covariance  
491 matrix of parameter values was used to estimate model uncertainty for each pixel. Random  
492 vectors were generated from a multinomial normal distribution to create a set of 1000

493 realizations of the model parameters. These were then used to estimate 1000 realizations of  
494 biomass estimates. Assuming an unbiased estimator we define an interval from this resulting  
495 distribution for which the true mean response is within. We do not explicitly account for the  
496 random error of a new observation when calculating this interval, only the uncertainty in the  
497 mean of the population.

498 For the GEDI biomass estimates, the pixel underlying each GEDI simulated waveform centroid  
499 was used as reference. To filter footprints with spatial mismatches to the reference map (e.g. where  
500 only half a pixel is covered by GEDI) we implemented a height filter, where maximum forest  
501 height from the 30 m underlying pixel was compared to the RH99 value for simulated GEDI  
502 waveforms, calculated above ALS ground (e.g. not filtering waveforms that may have ground  
503 issues, but only those where the spatial coverage of footprints did not capture the underlying 30 m  
504 maximum height). We filtered out any waveform where this RH99 value was more than 5 m  
505 different than the underlying ALS 30 m height map.

506

507 For ICESat-2, the three pixels underlying the 100 m ICESat-2 transect were extracted and averaged  
508 for reference. For NISAR, all of the reference pixels were averaged at a 1 ha resolution for  
509 comparison to L-band backscatter estimates, and there was no spatial mismatch because of the  
510 wall-to-wall sampling of the SAR data.

511

512 The statistical comparison of simulated spaceborne estimates to reference estimates was conducted  
513 by computing confidence intervals around both sets of predictions. In reference pixels with high  
514 uncertainties, we are unable to ‘validate’ the spaceborne estimates; indeed, if the confidence  
515 intervals between the ALS and simulated spaceborne estimates overlap, there is no discernable

516 error in the spaceborne estimates insofar as the reference map can detect. This does not, however,  
517 mean the spaceborne estimate is without error. Conversely, if there is no overlap between these  
518 90<sup>th</sup> percentile confidence intervals, (i.e. the minimum from the reference map is still greater than  
519 the maximum from the spaceborne estimate) we can determine that the uncertainties in the  
520 spaceborne estimate are underestimated. In sum, we can only validate that spaceborne estimates  
521 are correct to the accuracy level of the reference map, but we can determine when spaceborne  
522 estimates are definitively incorrect. To achieve this, we calculated the percentage of estimates for  
523 each mission that had per pixel overlapping confidence intervals with the corresponding reference  
524 map, and attempted to explain observe errors as a function of environment. This is reported in  
525 addition to more traditional differences in means between reference and spaceborne estimates.

526

527 In addition to biomass estimates, the county-wide airborne lidar dataset was used to generate 30  
528 m resolution maps of terrain slope, forest canopy height and percent canopy cover. These maps  
529 were used to assess the impact of these variables on biomass estimation accuracy. The slope,  
530 height, and cover maps were extracted to match the simulated spaceborne resolutions the same  
531 way the biomass map was used for comparison. For the comparison of NISAR estimates to slope  
532 we used SAR observed slope rather than absolute slope, as the SAR signals are affected by  
533 topography depending on the look angle of the sensor, with topography either facing away from  
534 the sensor (typically decreasing backscatter) or toward the sensor (typically increasing  
535 backscatter).

536

537 **3.5 Comparison of ICESat-2 and GEDI height metrics**

538 To explore the utility of GEDI's biomass algorithms to ICESat-2 data, we also simulated GEDI  
539 footprints at the midpoint of ICESat-2 100-m transects across Sonoma. Considering differences  
540 between GEDI and ICESat-2 instruments and datasets (wavelength, spatial resolution,  
541 calculation of RH metrics, etc.) we calculated the biases between RH95, RH75, RH50 and  
542 RH25 between simulations of GEDI's power beam collected in nighttime (low noise) conditions,  
543 and the two sets of ICESat-2 simulations. We also compared the ALS heights to GEDI and  
544 ICESat-2 estimated heights following the same approach for extracting reference values as for  
545 the biomass evaluation, and compared residuals as a function of environment.  
546

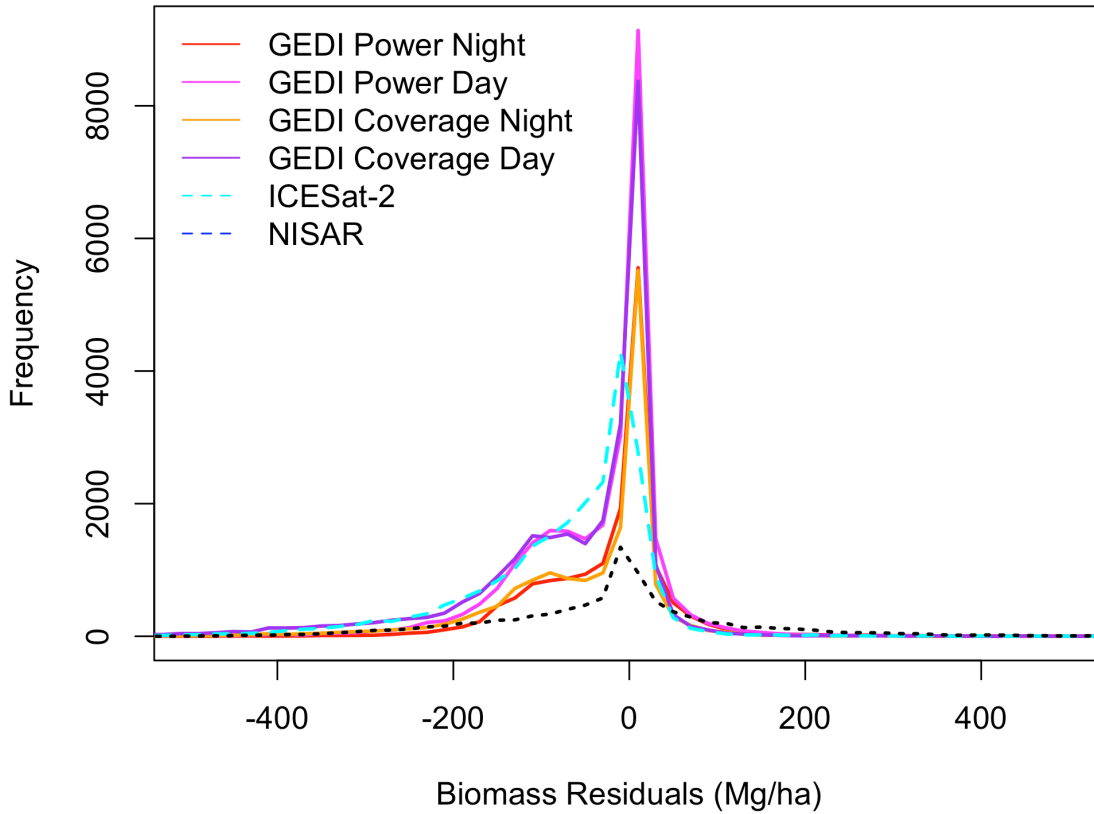
547 **4.0 Results**

548 The biomass residuals from the three simulated missions (Fig 9), as calculated by comparison to  
549 the ALS reference map at their nominal resolutions, vary as a function of maximum canopy height,  
550 percent canopy cover, and terrain slope (Fig 10). Note that Fig 9 and 10 include all estimates,  
551 regardless of whether there were overlapping confidence intervals. The relative accuracies of each  
552 of these datasets is presented in Table 2 with respect to the ALS reference estimates at each  
553 resolution, where the % confidence interval overlap is the percentage of estimates where the 90<sup>th</sup>  
554 percentile confidence intervals from the reference and spaceborne estimates overlap, RMSE is the  
555 square root of the mean squared residuals, mean bias is calculated as the mean residuals (with  
556 respect to the ALS map), %RMSE and % bias divides these statistics by the mean reference  
557 biomass at each resolution, and slope is the slope of a linear model fit between spaceborne  
558 estimates and the reference map. The distance between the extremes of the reference confidence  
559 interval and simulated spaceborne confidence intervals are also dependent on environmental  
560 gradients (SI Fig 2). As expected, GEDI errors also increase as a function of biomass, with higher  
561 sensitivity of errors to biomass seen in daytime and coverage beam simulations (Fig 11). ICESat-  
562 2 errors are also sensitive to biomass, particularly for the low photon rate simulations (Fig 12).  
563 We also compared the realistic ICESat-2 rate height metrics to simulated GEDI height metrics at  
564 the same locations to explore limitations to the transferability of GEDI's models to ICESat-2, and  
565 found that particularly for the low photon rate biases between the two sets of height metrics likely  
566 limit the accuracy of ICESat-2 for biomass estimation using this approach (Fig 13). However, we  
567 also found that ICESat-2 and GEDI coverage beams underestimated height particularly in tall  
568 forests (Fig SI5), suggesting biomass estimation for weaker beams is primarily limited by height  
569 estimation regardless of the biomass model selection.

570 **Table 2. Assessment of each simulated mission dataset calculated with respect to the**  
 571 **reference airborne lidar biomass map at 30m (GEDI), 3x30 m (ICESat-2), and 1 ha (NISAR).**

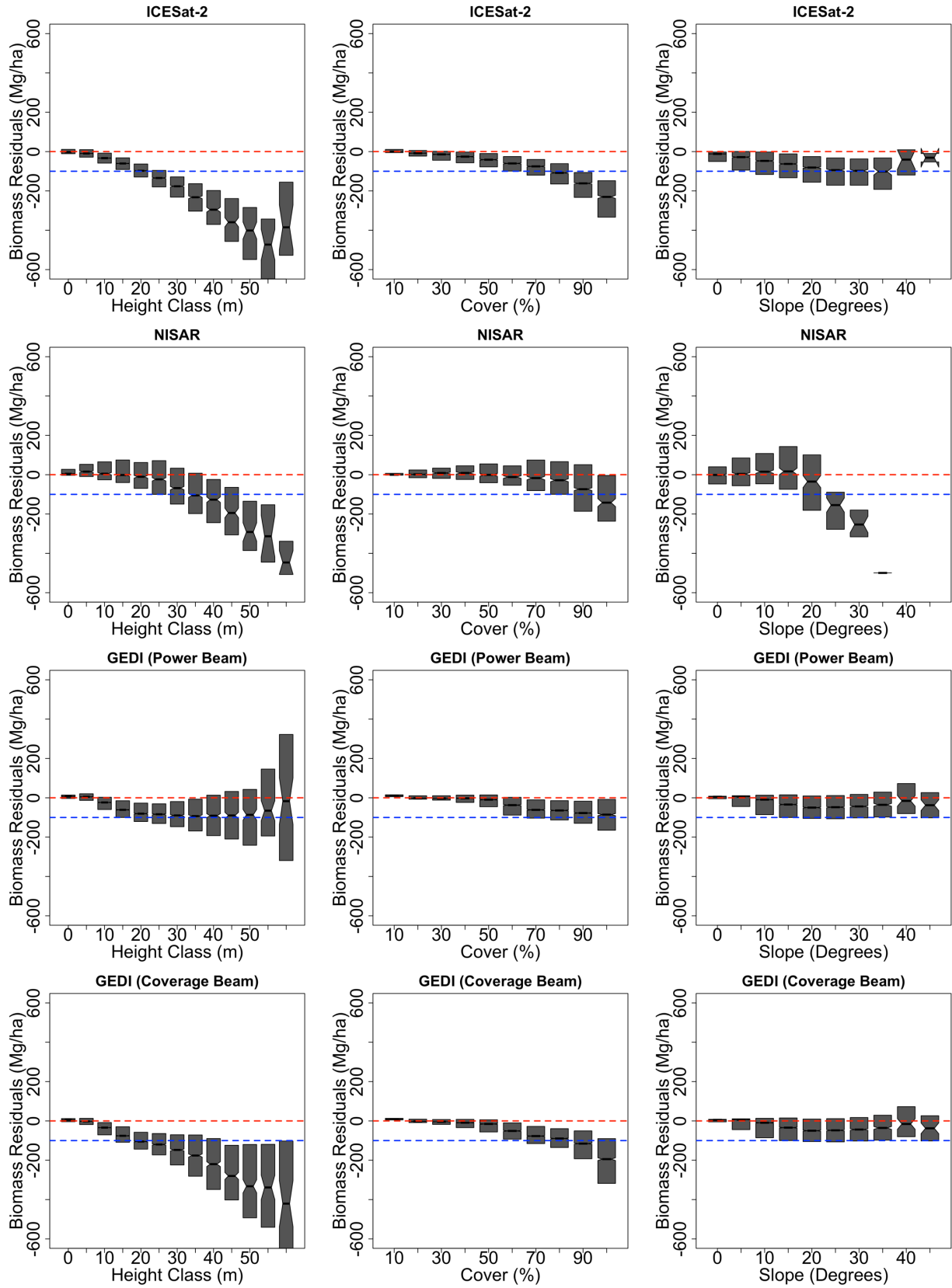
<b>Mission</b>	<b>Scenario</b>	<b>%Confidence Overlap</b>	<b>RMSE (Mg/ha)</b>	<b>%RMSE (Mg/ha)</b>	<b>Mean Bias (Mg/ha)</b>	<b>%Bias Mean</b>	<b>Slope</b>
<b>GEDI</b>	Power night	58.4	80.2	57.1	-26.3	-18.7	0.81
<b>GEDI</b>	Power day	56	93.1	64.5	-38	-26.3	0.72
<b>GEDI</b>	Coverage night	54.2	105.5	71.7	-47.8	-32.5	0.64
<b>GEDI</b>	Coverage day	50.8	128.8	87.6	-64.2	-43.7	0.49
<b>NISAR</b>	All bio	34.6	151.55	74.9	-7.47	-0.03	0.73
<b>NISAR</b>	Low bio	46.5	101.7	288	-37.4	-0.5	0.17
<b>ICESat-2</b>	High photon return	47.6	106.4	59	-23.34	-13%	0.69
<b>ICESat-2</b>	Low photon return	34.9	137.8	89.1	-72.11	-47%	0.4

572

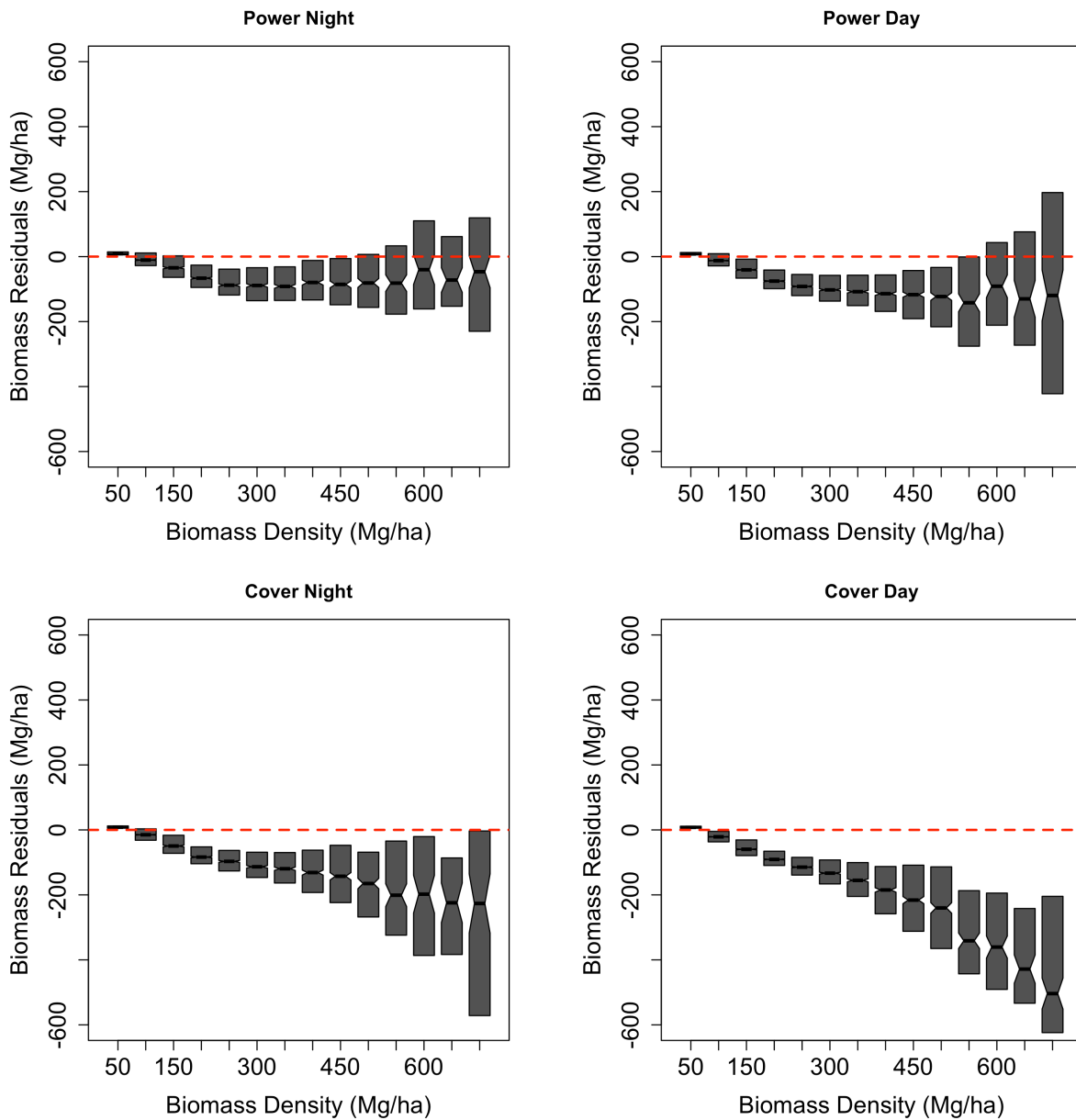


573

574 **Fig 9 Histograms showing the relative distribution of residuals (simulated mission**  
 575 **estimates in comparison to the reference biomass map) from each mission. Note that here**  
 576 **low-photon rate ICESat-2 simulations were used.**



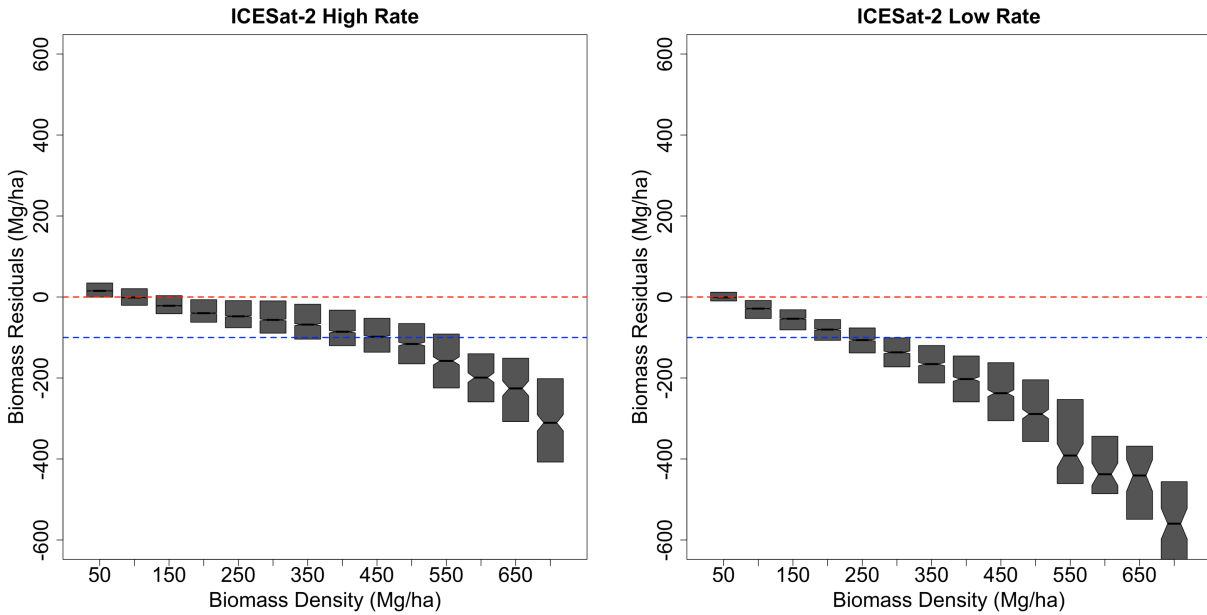
578 **Fig 10 ICESat-2 residuals (a-c), NISAR residuals (d-f), GEDI power beam residuals (g-i),**  
 579 **and GEDI coverage beam residuals (j-l) plotted as a function of canopy height, % canopy**  
 580 **cover, and slope. Each mission's residuals are presented with respect to ALS estimated**  
 581 **biomass at their native resolution, i.e. footprint-level (25 m) for GEDI, 100 m transects for**  
 582 **ICESat-2, and 1 ha for NISAR (UAVSAR). The blue dotted lines are plotted for**  
 583 **comparison at negative 100 Mg/ha of biomass. The blue dotted line represents -100 Mg/ha.**



584

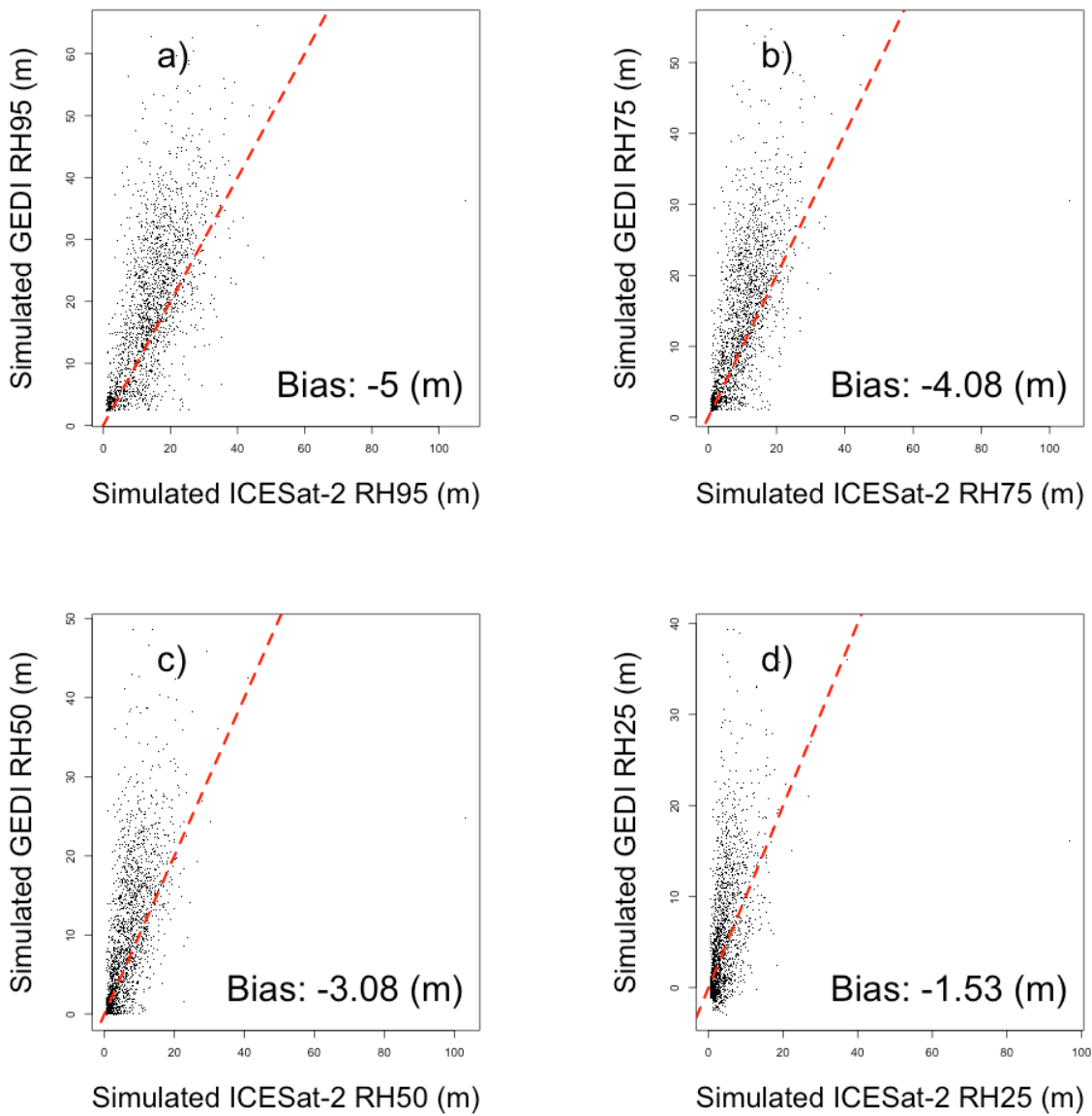
585 **Fig 11 Simulated GEDI biomass residuals as a function of reference biomass bin, plotted**  
586 **for each of our four GEDI simulation scenarios.**

587



588

589 **Fig 12 Higher signal photon rates for ICESat-2 (a) decrease biomass estimations by ~50%**  
590 **in each reference biomass bin, but even high photon rates still yield underestimates of**  
591 **biomass beyond ~500 Mg/ha. The blue dotted line represents -100 Mg/ha.**



592

593 **Fig 13. A comparison of simulated GEDI RH metrics to the lower signal photon return rate**

594 **ICESat-2 estimations shows that ICESat-2 underestimates height, particularly in the**

595 **higher height metrics (e.g. RH95). These underestimates of height partially explain**

596 **underestimates of biomass from simulated ICESat-2.**

597

598

599 **4.1 GEDI Biomass Residuals**

600 GEDI's power beam biomass estimates yield the lowest deviations from the reference map both  
601 on average and in high biomass, tall, dense forests compared to any other simulated spaceborne  
602 estimate in this study. The power beam also has the highest percentage of overlapping confidence  
603 intervals, indicating that not only are the mean values closest to the reference values, but the  
604 uncertainties estimated for the GEDI power beam data were accurately reported almost 60% of the  
605 time. On average, the GEDI power beam data still slightly underestimates biomass in Sonoma  
606 County, but these underestimates are modest across ranges of topography and forest structure. A  
607 comparison between the GEDI power and coverage beams, Figs 10, 12, and SI5, suggests that the  
608 majority of errors in simulated GEDI biomass estimates come from errors in the height metric  
609 estimates in the coverage beam data rather than errors in the GEDI biomass model. Additionally,  
610 topographic slope does not appear to drive errors in either the power or coverage beam data (Fig  
611 10, SI5).

612

613 **4.2 NISAR Biomass Residuals**

614 While NISAR residuals are generally unbiased in areas of low canopy cover and slope, over slopes  
615 steeper than ~20 degrees or forests taller than ~25 m NISAR underestimates biomass by more than  
616 100 Mg/ha (Fig 10), with increasing underestimation in taller forests or over steeper slopes. These  
617 errors are likely due to saturation issues in the backscatter signal, as expected for L-band SAR, but  
618 the good performance in shorter, lower canopy cover forests shows promise for the utility of fusion  
619 algorithms to extend lidar samples toward wall-to-wall mapping.

620

621 **4.3 ICESat-2 Biomass Residuals**

622 For ICESat-2, we focus our analysis on the lower signal photon rate simulations because they  
623 match the photon rates of the limited on-orbit ICESat-2 data that have been collected over Sonoma  
624 County at the time of writing. As seen in Fig 10, ICESat-2 underestimates biomass on average,  
625 and this underestimation increases with canopy height, canopy cover, and to a small degree with  
626 slope. The comparison between simulated GEDI and ICESat-2 height metrics (Fig 13) confirms  
627 that at least with respect to GEDI simulations, ICESat-2 underestimates height, and these  
628 underestimations are more pronounced in the higher height metrics. Further, Fig SI5 shows that  
629 the same trends in height error with respect to ALS height match the trends found in biomass  
630 estimation errors. However, a comparison of ICESat-2 simulations from the higher signal photon  
631 return rate (SI Fig 3) shows that the signal rate drives much of this error, so in areas where ICESat-  
632 2 has little atmospheric attenuation ICESat-2 will likely perform well for forest structure.

633

## 634 **5.0 Discussion**

### 635 **5.1 Utility of Airborne Lidar Reference Maps for Validation**

636 Our multi-mission inter-comparison depended entirely on the availability of a high-quality  
637 regional reference map that is trained with field data across the range of conditions found in  
638 Sonoma County. The spatial configuration of both NISAR and ICESat-2 mean that field plots are  
639 typically not readily available for direct comparison to spaceborne missions. Even for GEDI, when  
640 small field plots are available, geolocation errors in the field data and/or GEDI data will add errors  
641 to the calibration and validation process (Réjou-Méchain et al., 2019). Airborne lidar is an ideal  
642 tool for scaling between field plots and satellite datasets, as has been widely documented.  
643 Additional advantages highlighted in this study are the ability to explain errors in satellite datasets  
644 as a function of structural gradients, both of vegetation and the underlying terrain. Further, the

645 ability to aggregate high resolution lidar biomass maps to the appropriate spatial resolution of a  
646 given satellite product allows for the comparison of multi-mission datasets over the same set of  
647 environmental conditions, enabling a more thorough evaluation of the strengths and limitations of  
648 each dataset toward informed data fusion.

649

650 While ALS biomass maps allow for simple scaling to multiple mission resolutions, the  
651 interpretation of the results in this paper should be caveated by the different spatial scales analyzed.  
652 It is well accepted that biomass model fitting errors reduce with increasing plot size or resolution  
653 (Hall et al., 2011; Labriere et al., 2018; Zolkos et al., 2013), partially because of reductions in edge  
654 effects, but largely because of the reduced variance in the biomass values with increases in spatial  
655 scale. Therefore, the results in this study cannot be directly quantitatively compared because the  
656 estimation and validation were at three different resolutions. Additionally, our airborne biomass  
657 estimates only accounted for uncertainty in the mean of the population and ignored the uncertainty  
658 in individual observations. There remain a lack of studies that comprehensively account for  
659 sources of measurement and model error in spaceborne estimates and ALS reference maps for such  
660 comparisons. A review of existing methods and recommendations for best practice are currently  
661 the subject of the forthcoming CEOS LPV Biomass validation protocol (Duncanson et al., 2019).

662

663 This research involved the utility of airborne lidar biomass maps for validation, and focused on  
664 understanding expected errors in biomass products from upcoming GEDI, ICESat-2 and NISAR  
665 datasets, and there are several important caveats in the interpretation of this work. First, we present  
666 a simplified version of simulated estimates from three sensors and this work is not fully  
667 representative of finalized mission algorithms. Trends between errors and environmental gradients

668 will differ for other areas, e.g. in different forest types such as in the tropics. Additionally, although  
669 we expect mission algorithms to be generally similar to those adopted here, the final GEDI models  
670 and ground finding algorithms will likely vary in specificity, variable selection, parameterization,  
671 and ultimately accuracy. The NISAR models, similarly, will differ from those shown here, as they  
672 will be generalized across biomes rather than locally fit, focused on relatively simpler, lower  
673 biomass systems than those in this study, and be based on temporal composites of L-band  
674 backscatter rather than the single date UAVSAR data used in this study.

675

## 676 **5.2 Interpretation of Simulated Mission Biomass Estimation Accuracies**

677 In this paper we focus on developing and implementing algorithms as similar as currently  
678 possible to those used by mission teams to produce biomass estimates at the aforementioned  
679 resolutions, although we expect a large number of researchers will develop their own biomass  
680 algorithms for particular applications. Thus, these algorithms can be thought of as reasonable  
681 approximations for expected estimates of biomass from the upcoming missions, but by no means  
682 represent the only approach one may take to estimate biomass with GEDI, ICESat-2, or NISAR.  
683 Similarly, neither of the simulated lidar mission datasets are used here to produce a gridded  
684 product akin to what the mission teams will release, but can be thought of as similar to what  
685 GEDI's footprint level biomass product will produce, and similar to a possible transect-level  
686 product from ICESat-2.

687

688 Overall, these upcoming missions performed as one might expect in such a challenging, high  
689 biomass system. Sonoma County presents a wide range of biomass densities, with the mean  
690 biomass far above the expected saturation limit for optical and even L-band SAR systems. As

691 such, we anticipated saturation in the NISAR simulations, and high RMSE values for the lidar  
692 systems. In addition to high biomass densities, the steep slopes found in much of Sonoma  
693 increase errors in height retrievals and biomass estimates, which was also expected. Considering  
694 the application of generalized biomass models to these spaceborne lidar simulations, we find  
695 these results are generally in line with expected mission performance, and feel they highlight  
696 environmental domains that will remain challenging for this next generation of datasets. Indeed,  
697 we feel this study highlights areas where further research and algorithm refinement would be  
698 particularly beneficial.

699

700 We found that for the lidar missions, height retrieval accuracy was the primary driver of biomass  
701 error estimation, with errors more highly related to forest structure than to terrain slope. As  
702 expected, the highest accuracies were from GEDI's power beam, while accuracies for ICESat-2  
703 depended heavily on the signal photon rate, and NISAR accuracies will depend on the availability  
704 of high-quality biomass training data, and be limited to lower biomass forests over relatively flat  
705 areas. Nonetheless, we find all three sets of mission simulations promising for biomass. From a  
706 GEDI perspective, the simulated estimates had the highest accuracies as expected and certainly  
707 performance is well within mission requirements. Considering that Sonoma County hosts some of  
708 the highest biomass densities in the United States, many of which are growing over steep slopes,  
709 this is indeed an encouraging result. As expected, errors in GEDI heights, and therefore biomass  
710 estimates increase for the coverage beams, particularly when acquired during the daytime.

711

712 Also encouraging is the relative success of applying GEDI's footprint level biomass algorithms to  
713 ICESat-2. As ICESat-2 does not have a mission requirement for forest structure or biomass, this

714 ICESat-2 work was largely exploratory, and Sonoma County presents an interesting test bed for  
715 ICESat-2. It is important to note that while we adapted GEDI's algorithms to only consider RH  
716 metrics available in the ICESat-2 vegetation product for model development, these models were  
717 fit at the GEDI resolution, not the ICESat-2 resolution, and for a robust development of ICESat-2  
718 models we would recommend fitting models at the ICESat-2 resolution. Unfortunately,  
719 considering that few field plots exist that are large enough, and stem-mapped to enable extraction  
720 of 100m by 13 m plots, we expect ICESat-2 model development will either involve adaption of  
721 GEDI's models (as in this study), or leverage high resolution, locally calibrated ALS biomass maps  
722 that enable the extraction of any reference size and shape. As expected, ICESat-2 underestimates  
723 heights, particularly in dense, tall forests, and therefore may not be appropriate for biomass  
724 mapping under all conditions. As with GEDI's coverage beam acquired during the day, it may be  
725 desirable to filter ICESat-2 data in dense forests. Based on our analysis, we would recommend  
726 caution when using low photon return rate ICESat-2 for biomass estimation in areas of  $>\sim 60\%$   
727 canopy cover. However, as seen in Fig 3, the spatial pattern of ICESat-2 is complementary to  
728 GEDI, and thus even a subset of ICESat-2 data should bolster fused forest structure mapping  
729 activities, particularly in areas with relatively open canopies (e.g. woodlands, plantations, alpine  
730 and boreal forests). In this study, high photon return rate ICESat-2 simulations could adequately  
731 detect the ground for biomass estimation, which shows promise for the utility of ICESat-2 even in  
732 areas of high biomass. However, other biomass rich areas such as the tropics may present greater  
733 difficulties. Ecosystem requirements for biomass as explained in (Hall et al., 2011) have specified  
734 that accuracies of about 1 m in height will be required for many science applications. Thus, further  
735 research should focus on how to reduce these biases, especially with an eye towards the eventual

736 creation of blended GEDI/ICESat-2 height products, and any biomass products generated from  
737 these.

738

739 While the sampling lidar missions show tremendous promise toward accurate global forest  
740 structure datasets, many applications (e.g. for land managers) require wall-to-wall mapping. Our  
741 NISAR results are also encouraging, in that L-band SAR data were able to estimated biomass even  
742 in relatively dense canopies (up to ~70% canopy cover), which corresponds roughly to 100 Mg/ha  
743 in Sonoma, approximately the expected saturation limit of L-band backscatter. It should be re-  
744 emphasized that for our NISAR simulations, the biomass estimates in this study were trained with  
745 the reference biomass map, and therefore biases were not realistically assessed, we anticipate that  
746 NISAR biomass estimates will likely be trained with GEDI (and potentially ICESat-2) in the  
747 future. Even using the simplistic methods adopted here would enable the extension of the lidar  
748 samples to wall-to-wall maps, and we fully anticipate more sophisticated approaches will be  
749 developed once NISAR data are available to the scientific community.

750

751 When looked at as an ensemble of observations, the combination of all three mission datasets  
752 potentially provides an interesting range of capabilities that spans high biomass, high cover and  
753 repeated and global coverage. When used together, there is the potential to generate biomass  
754 products that are more accurate and/or of higher resolution than what any one mission could  
755 produce by itself. But as noted above, an informative first step is a comparison of biomass  
756 estimation errors from all three missions separately, as conducted in this paper. The methods  
757 presented here allow interpretation of biomass estimation errors from these three simulated

758 mission datasets over the same range of environmental conditions, allowing a comparison of the  
759 general strengths and weaknesses of each.

760

## 761 **6.0 Conclusions**

762 We are entering an exciting era for active remote sensing of forests, with a wealth of upcoming  
763 datasets sensitive to forest structure. We anticipate many new forest biomass products will be  
764 generated through various combinations of these next generation datasets, and while this is  
765 desirable, the consistent comparison of forthcoming products is critical to the continued  
766 improvement of algorithms and adoption of products for a wide range of applications. This paper  
767 focuses on comparing simulated biomass estimates from three new and upcoming missions, GEDI,  
768 ICESat-2 and NISAR, that will each collect a different type of data useful to varying degrees for  
769 biomass mapping. Although ICESat-2 does not have a mission science requirement of biomass  
770 products, and NISAR only has a requirement to be able to estimate biomass less than 100 Mg/ha,  
771 we have explored the impact of topography and forest structure on estimating biomass from each  
772 of these missions, focusing on a structurally complex temperate forested ecosystem. Our results  
773 have shown that each mission, by itself, will perform differently under varying environmental  
774 conditions, which was expected. Only one of the missions, GEDI, was specifically designed to  
775 retrieve vegetation structure and biomass under a large range of environmental conditions  
776 sufficient to meet biomass mapping requirements as specified by the ecosystem community.  
777 However, both NISAR and ICESat-2 will provide exceptionally valuable observations for biomass  
778 mapping, providing global observations, and in the case of NISAR all-weather capability and very  
779 high-temporal resolution. One needs only to look at the examples of ALOS PALSAR and ICESat  
780 (GLAS) to understand the impact that missions, whose main foci are not ecosystem structure, may

781 have on biomass mapping.

782

783 Looking forward, it is reasonable to expect users to want to use the data from all three missions  
784 for various applications. Whether they should use all the data is a different question and will rest  
785 in large part on how well the errors of using any particular data set can be characterized. Until all  
786 three missions are in orbit and collecting data, we will not know for certain what the true capability  
787 of each system is, nor how this may change with time. In this sense, our work provides a preview  
788 of what might influence the accuracy of each data product, and what an end-user might expect  
789 when evaluating whether to embark along a path of multi-sensor mapping using GEDI, NISAR  
790 and ICESat-2.

791

## 792 **Acknowledgements**

793 This work was primarily funded through NASA's Carbon Monitoring System (CMS, grant 15-  
794 CMS15-0055), and the authors gratefully acknowledge additional support for coauthors  
795 Hancock, Armston, Kellner and Dubayah by a NASA contract to the University of Maryland for  
796 the Global Ecosystem Dynamics Investigation, and additional support for Amy Neuenschwander  
797 through ICESat-2 (NASA HQ NNX17AG55G). This work involved significant contributions  
798 from many other individuals on mission teams, and we would like to particularly thank Paul  
799 Patterson and Sean Healey for helpful input in the development of the lidar biomass models  
800 applied here. We also gratefully acknowledge Mike Falkowski, Andy Hudak, Patrick Fakety,  
801 Warren Cohen, Hans Anderson, and Luigi Boscetti for provision of the US field and airborne  
802 lidar used to generate the lidar algorithms in this study (published in a separate paper), and  
803 Suzanne Marselis and David Minor for data processing and database management. Additional

804 thanks to Kaitlin Harbeck for helping produce the simulated ICESat-2 data, and Katherine Pitts  
805 for running the ATL08 algorithm on the simulated ICESat-2 data.

806

## 807 **References**

- 808 Baccini, A., Goetz, S.J., Walker, W.S., Laporte, N.T., Sun, M., Sulla-Menashe, D., Hackler, J.,  
809 Beck, P.S.A., Dubayah, R., Friedl, M.A., Samanta, S., Houghton, R.A., 2012. Estimated  
810 carbon dioxide emissions from tropical deforestation improved by carbon-density maps.  
811 *Nat. Clim. Change* 2, 182–185. <https://doi.org/10.1038/nclimate1354>
- 812 Blair, J.B., Hofton, M.A., 1999. Modeling laser altimeter return waveforms over complex  
813 vegetation using high-resolution elevation data. *Geophys. Res. Lett.* 26, 2509–2512.  
814 <https://doi.org/10.1029/1999GL010484>
- 815 Chave, J., Réjou-Méchain, M., Búrquez, A., Chidumayo, E., Colgan, M.S., Delitti, W.B.C.,  
816 Duque, A., Eid, T., Fearnside, P.M., Goodman, R.C., Henry, M., Martínez-Yrizar, A.,  
817 Mugasha, W.A., Muller-Landau, H.C., Mencuccini, M., Nelson, B.W., Ngomanda, A.,  
818 Nogueira, E.M., Ortiz-Malavassi, E., Pélissier, R., Ploton, P., Ryan, C.M., Saldarriaga,  
819 J.G., Vieilledent, G., 2014. Improved allometric models to estimate the aboveground  
820 biomass of tropical trees. *Glob. Change Biol.* 20, 3177–3190.  
821 <https://doi.org/10.1111/gcb.12629>
- 822 Chen, Q., 2010. Retrieving vegetation height of forests and woodlands over mountainous areas  
823 in the Pacific Coast region using satellite laser altimetry. *Remote Sens. Environ.* 114,  
824 1610–1627. <https://doi.org/10.1016/j.rse.2010.02.016>
- 825 Clark, D.B., Kellner, J.R., 2012. Tropical forest biomass estimation and the fallacy of misplaced  
826 concreteness. *J. Veg. Sci.* 23, 1191–1196. [https://doi.org/10.1111/j.1654-](https://doi.org/10.1111/j.1654-1103.2012.01471.x)  
827 [1103.2012.01471.x](https://doi.org/10.1111/j.1654-1103.2012.01471.x)
- 828 Clewley, D., Bunting, P., Shepherd, J., Gillingham, S., Flood, N., Dymond, J., Lucas, R.,  
829 Armston, J., Moghaddam, M., 2014. A Python-Based Open Source System for  
830 Geographic Object-Based Image Analysis (GEOBIA) Utilizing Raster Attribute Tables.  
831 *Remote Sens.* 6, 6111–6135. <https://doi.org/10.3390/rs6076111>
- 832 Davidson, F.M., Sun, X., 1988. Gaussian approximation versus nearly exact performance  
833 analysis of optical communication systems with PPM signaling and APD receivers. *IEEE*  
834 *Trans. Commun.* 36, 1185–1192. <https://doi.org/10.1109/26.8924>
- 835 Drake, J.B., Dubayah, R.O., Knox, R.G., Clark, D.B., Blair, J.B., 2002. Sensitivity of large-  
836 footprint lidar to canopy structure and biomass in a neotropical rainforest. *Remote Sens.*  
837 *Environ.* 81, 378–392.
- 838 Dubayah, R., Swatantran, A., Huang, W., Duncanson, L., Tang, H., Johnson, K., Hurtt, G.C.,  
839 2013. CMS: LiDAR-derived Biomass, Canopy Height and Cover, Sonoma County,  
840 California, 2013.
- 841 Duncanson, L., Armston, J., Disney, M., Avitabile, V., Barbier, N., Calders, K., Carter, S.,  
842 Chave, J., Herold, M., Crowther, T.W., Falkowski, M., Kellner, J.R., Labrière, N., Lucas,  
843 R., MacBean, N., McRoberts, R.E., Meyer, V., Næsset, E., Nickeson, J.E., Paul, K.I.,  
844 Phillips, O.L., Réjou-Méchain, M., Román, M., Roxburgh, S., Saatchi, S.,  
845 Schepaschenko, D., Scipal, K., Siqueira, P.R., Whitehurst, A., Williams, M., 2019. The  
846 Importance of Consistent Global Forest Aboveground Biomass Product Validation. *Surv.*  
847 *Geophys.* 40, 979–999. <https://doi.org/10.1007/s10712-019-09538-8>

848 Duncanson, L., Huang, W., Johnson, K., Swatantran, A., McRoberts, R.E., Dubayah, R., 2017.  
849 Implications of allometric model selection for county-level biomass mapping. *Carbon*  
850 *Balance Manag.* 12. <https://doi.org/10.1186/s13021-017-0086-9>  
851 Duncanson, L.I., Niemann, K.O., Wulder, M.A., 2010. Estimating forest canopy height and  
852 terrain relief from GLAS waveform metrics. *Remote Sens. Environ.* 114, 138–154.  
853 <https://doi.org/10.1016/j.rse.2009.08.018>  
854 Hall, F.G., Bergen, K., Blair, J.B., Dubayah, R., Houghton, R., Hurtt, G., Kelldorfer, J., Lefsky,  
855 M., Ranson, J., Saatchi, S., Shugart, H.H., Wickland, D., 2011. Characterizing 3D  
856 vegetation structure from space: Mission requirements. *Remote Sens. Environ.* 115,  
857 2753–2775. <https://doi.org/10.1016/j.rse.2011.01.024>  
858 Hancock, S., Armston, J., Hofton, M., Sun, X., Tang, H., Duncanson, L.I., Kellner, J.R.,  
859 Dubayah, R., 2019. The GEDI simulator: A large-footprint waveform lidar simulator for  
860 calibration and validation of spaceborne missions. *Earth Space Sci.*  
861 <https://doi.org/10.1029/2018EA000506>  
862 Hancock, S., Disney, M., Muller, J.-P., Lewis, P., Foster, M., 2011. A threshold insensitive  
863 method for locating the forest canopy top with waveform lidar. *REMOTE Sens. Environ.*  
864 115, 3286–3297.  
865 Hilbert, C., Schmillius, C., 2012. Influence of Surface Topography on ICESat/GLAS Forest  
866 Height Estimation and Waveform Shape. *Remote Sens.* 4, 2210–2235.  
867 <https://doi.org/10.3390/rs4082210>  
868 Homer, C., Dewitz, J., Yang, L., Jin, S., Danielson, P., Xian, G., Coulston, J., Herold, N.,  
869 Wickham, J., Megown, K., 2015. Completion of the 2011 National Land Cover Database  
870 for the conterminous United States—representing a decade of land cover change  
871 information. *Photogramm. Eng. Remote Sens.* 81, 345–354.  
872 Houghton, R.A., House, J.I., Pongratz, J., van der Werf, G.R., DeFries, R.S., Hansen, M.C., Le  
873 Quéré, C., Ramankutty, N., 2012. Carbon emissions from land use and land-cover  
874 change. *Biogeosciences* 9, 5125–5142. <https://doi.org/10.5194/bg-9-5125-2012>  
875 Huang, W., Swatantran, A., Duncanson, L., Johnson, K., Watkinson, D., Dolan, K., O’Neil-  
876 Dunne, J., Hurtt, G., Dubayah, R., 2017. County-scale biomass map comparison: a case  
877 study for Sonoma, California. *Carbon Manag.* 8, 417–434.  
878 <https://doi.org/10.1080/17583004.2017.1396840>  
879 Labriere, N., Tao, S., Chave, J., Scipal, K., Toan, T.L., Abernethy, K., Alonso, A., Barbier, N.,  
880 Bissiengou, P., Casal, T., Davies, S.J., Ferraz, A., Herault, B., Jaouen, G., Jeffery, K.J.,  
881 Kenfack, D., Korte, L., Lewis, S.L., Malhi, Y., Memiaghe, H.R., Poulsen, J.R., Rejou-  
882 Mechain, M., Villard, L., Vincent, G., White, L.J.T., Saatchi, S., 2018. In Situ Reference  
883 Datasets From the TropiSAR and AfriSAR Campaigns in Support of Upcoming  
884 Spaceborne Biomass Missions. *IEEE J. Sel. Top. Appl. Earth Obs. Remote Sens.* 1–11.  
885 <https://doi.org/10.1109/JSTARS.2018.2851606>  
886 Le Quéré, C., Andrew, R.M., Friedlingstein, P., Sitch, S., Pongratz, J., Manning, A.C.,  
887 Korsbakken, J.I., Peters, G.P., Canadell, J.G., Jackson, R.B., Boden, T.A., Tans, P.P.,  
888 Andrews, O.D., Arora, V.K., Bakker, D.C.E., Barbero, L., Becker, M., Betts, R.A., Bopp,  
889 L., Chevallier, F., Chini, L.P., Ciais, P., Cosca, C.E., Cross, J., Currie, K., Gasser, T.,  
890 Harris, I., Hauck, J., Haverd, V., Houghton, R.A., Hunt, C.W., Hurtt, G., Ilyina, T., Jain,  
891 A.K., Kato, E., Kautz, M., Keeling, R.F., Klein Goldewijk, K., Körtzinger, A.,  
892 Landschützer, P., Lefèvre, N., Lenton, A., Lienert, S., Lima, I., Lombardozzi, D., Metzl,  
893 N., Millero, F., Monteiro, P.M.S., Munro, D.R., Nabel, J.E.M.S., Nakaoka, S., Nojiri, Y.,  
894 Padín, X.A., Pregon, A., Pfeil, B., Pierrot, D., Poulter, B., Rehder, G., Reimer, J.,  
895 Rödenbeck, C., Schwinger, J., Séférian, R., Skjelvan, I., Stocker, B.D., Tian, H.,  
896 Tilbrook, B., van der Laan-Luijkx, I.T., van der Werf, G.R., van Heuven, S., Viovy, N.,  
897 Vuichard, N., Walker, A.P., Watson, A.J., Wiltshire, A.J., Zaehle, S., Zhu, D., 2017.

898 Global Carbon Budget 2017. *Earth Syst. Sci. Data Discuss.* 1–79.  
899 <https://doi.org/10.5194/essd-2017-123>

900 Luckman, A., Baker, J., Honzak, M., Lucas, R., 1998. Tropical forest biomass density estimation  
901 using JERS-1 SAR: Seasonal variation, confidence limits, and application to image  
902 mosaics. *Remote Sens. Environ.* 63, 126–139.

903 Magruder, L. A., Brunt, K., and Alonzo, M. (2020) ICESat-2 horizontal geolocation accuracy validation  
904 using ground-based corner cube retro-reflectors. *IEEE Transactions on geoscience and remote sensing*,  
905 TGRS-2019-01754, in revision.

906

907 Mitchard, E.T.A., Saatchi, S.S., Woodhouse, I.H., Nangendo, G., Ribeiro, N.S., Williams, M.,  
908 Ryan, C.M., Lewis, S.L., Feldpausch, T.R., Meir, P., 2009. Using satellite radar  
909 backscatter to predict above-ground woody biomass: A consistent relationship across  
910 four different African landscapes. *Geophys. Res. Lett.* 36.  
911 <https://doi.org/10.1029/2009GL040692>

912 Neuenschwander, A., Magruder, L., 2016. The Potential Impact of Vertical Sampling Uncertainty  
913 on ICESat-2/ATLAS Terrain and Canopy Height Retrievals for Multiple Ecosystems.  
914 *Remote Sens.* 8, 1039. <https://doi.org/10.3390/rs8121039>

915 Neuenschwander, A., Pitts, K., 2019. The ATL08 land and vegetation product for the ICESat-2  
916 Mission. *Remote Sens. Environ.* 221, 247–259. <https://doi.org/10.1016/j.rse.2018.11.005>

917 Pan, Y., Birdsey, R.A., Houghton, R., Kauppi, P., Kurz, W., Phillips, O.L., Shvidenko, A., Lewis,  
918 S.L., Canadell, J.G., Ciais, P., Jackson, R.B., Pacala, S.W., McGuire, D.A., Piao, S.,  
919 Rautiainen, A., Sitch, S., Hayes, D., 2011. A large and persistent carbon sink in the  
920 world's forests. *Science* 333, 984–988. <https://doi.org/10.1126/science.1204588>

921 Pan, Y., Birdsey, R.A., Phillips, O.L., Jackson, R.B., 2013. The Structure, Distribution, and  
922 Biomass of the World's Forests. *Annu. Rev. Ecol. Evol. Syst.* 44, 593–622.  
923 <https://doi.org/10.1146/annurev-ecolsys-110512-135914>

924 Patterson, P.L., Healey, S.P., Ståhl, G., Saarela, S., Holm, S., Andersen, H.-E., Dubayah, R.O.,  
925 Duncanson, L., Hancock, S., Armston, J., Kellner, J.R., Cohen, W.B., Yang, Z., 2019.  
926 Statistical properties of hybrid estimators proposed for GEDI—NASA's global ecosystem  
927 dynamics investigation. *Environ. Res. Lett.* 14, 065007. <https://doi.org/10.1088/1748-9326/ab18df>

928

929 Réjou-Méchain, M., Barbier, N., Coutron, P., Ploton, P., Vincent, G., Herold, M., Mermoz, S.,  
930 Saatchi, S., Chave, J., de Boissieu, F., Féret, J.-B., Takoudjou, S.M., Pélissier, R., 2019.  
931 Upscaling Forest Biomass from Field to Satellite Measurements: Sources of Errors and  
932 Ways to Reduce Them. *Surv. Geophys.* 40, 881–911. <https://doi.org/10.1007/s10712-019-09532-0>

933

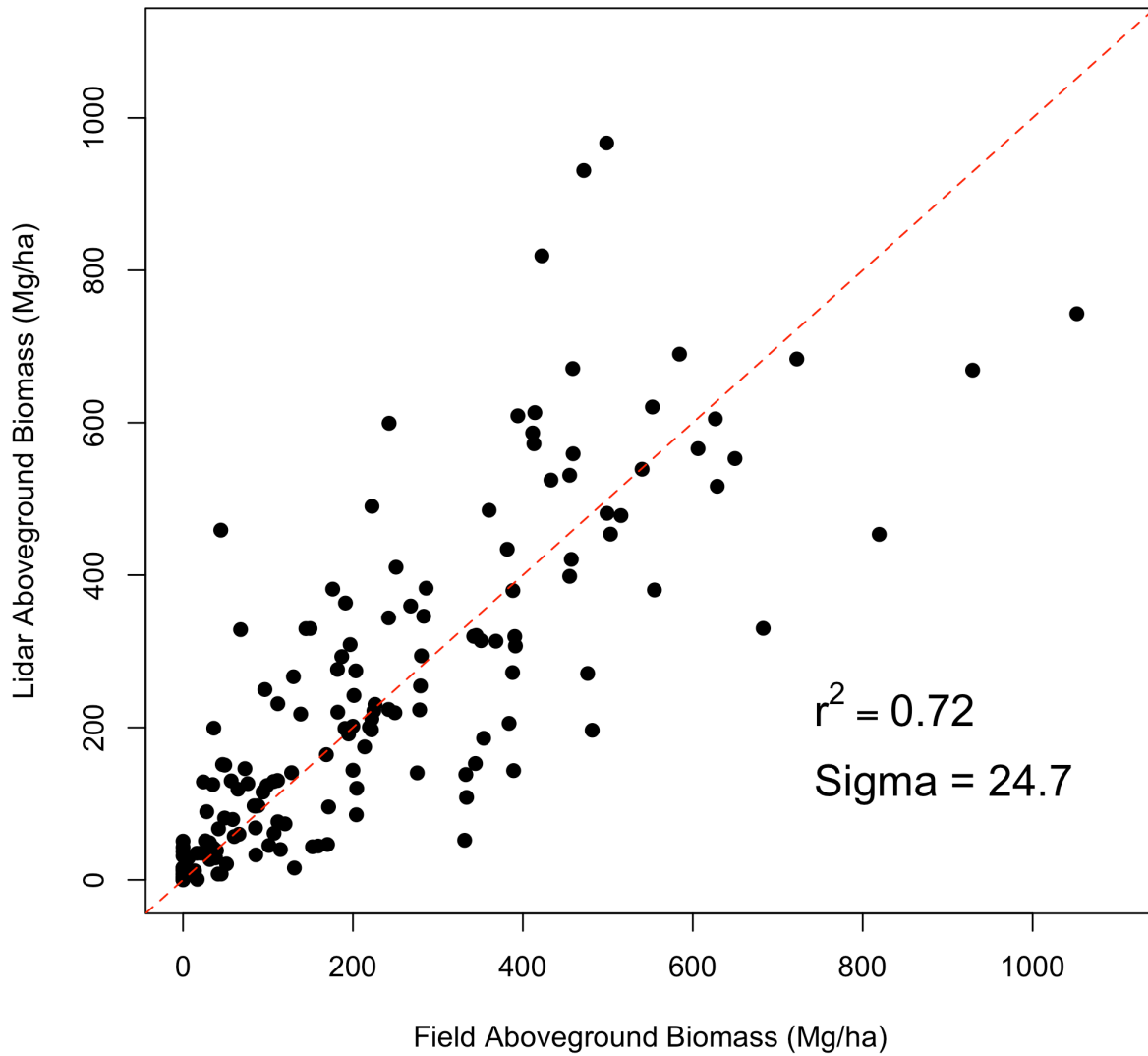
934 Rosen, P., Hensley, S., Shaffer, S., Edelstein, W., Kim, Y., Kumar, R., Misra, T., Bhan, R.,  
935 Satish, R., Sagi, R., 2016. An update on the NASA-ISRO dual-frequency DBF SAR  
936 (NISAR) mission, in: 2016 IEEE International Geoscience and Remote Sensing  
937 Symposium (IGARSS). Presented at the IGARSS 2016 - 2016 IEEE International  
938 Geoscience and Remote Sensing Symposium, IEEE, Beijing, China, pp. 2106–2108.  
939 <https://doi.org/10.1109/IGARSS.2016.7729543>

940 Saatchi, S.S., Harris, N.L., Brown, S., Lefsky, M., Mitchard, E.T., Salas, W., Zutta, B.R.,  
941 Buermann, W., Lewis, S.L., Hagen, S., others, 2011. Benchmark map of forest carbon  
942 stocks in tropical regions across three continents. *Proc. Natl. Acad. Sci.* 108, 9899–  
943 9904.

944 Simard, M., Riel, B.V., Denbina, M., Hensley, S., 2016. Radiometric Correction of Airborne  
945 Radar Images Over Forested Terrain With Topography. *IEEE Trans. Geosci. Remote*  
946 *Sens.* 54, 4488–4500. <https://doi.org/10.1109/TGRS.2016.2543142>

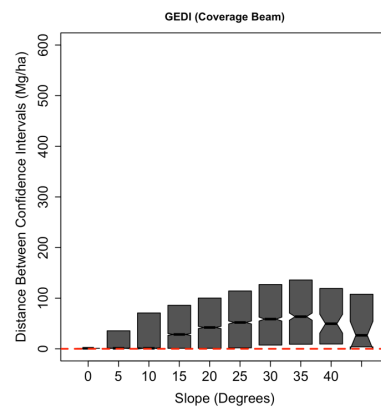
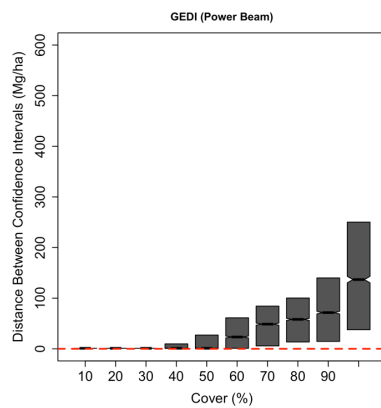
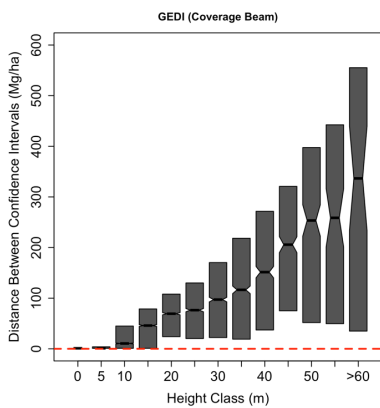
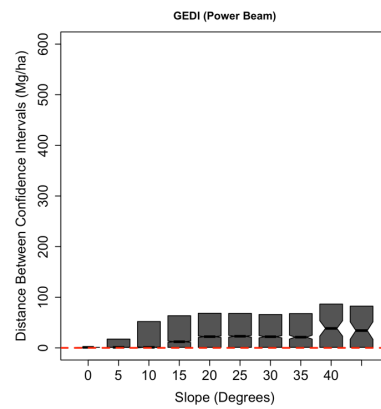
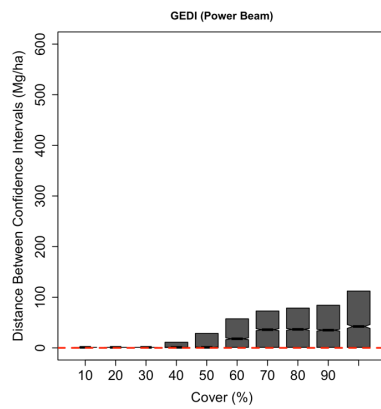
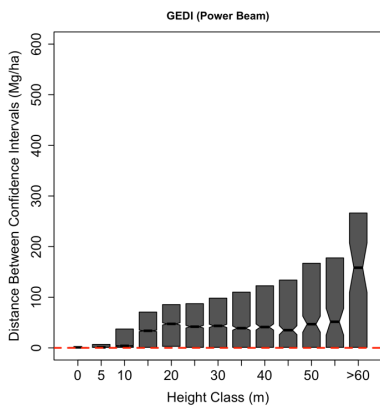
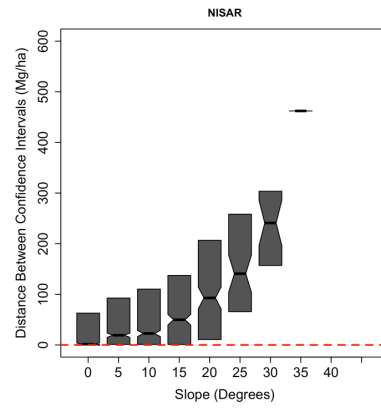
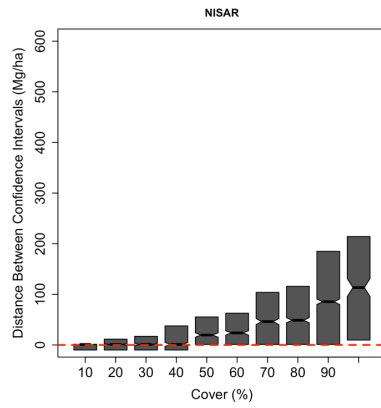
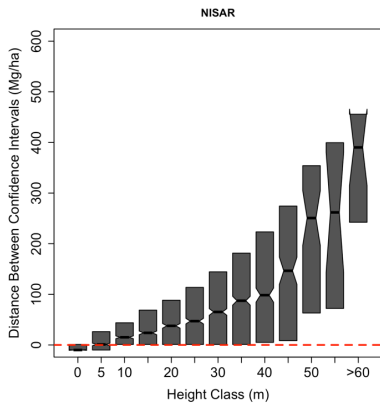
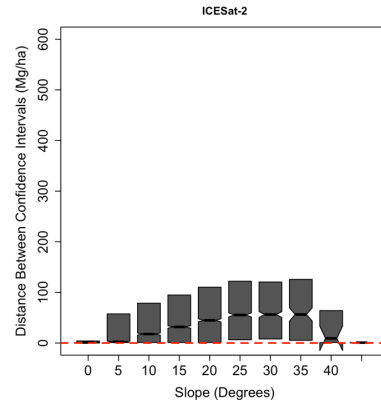
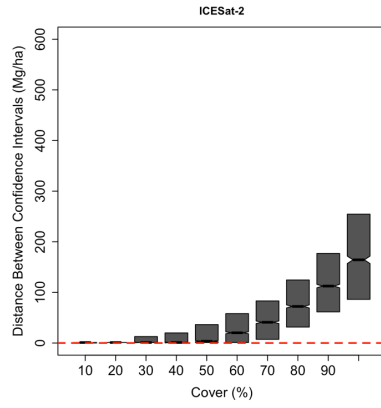
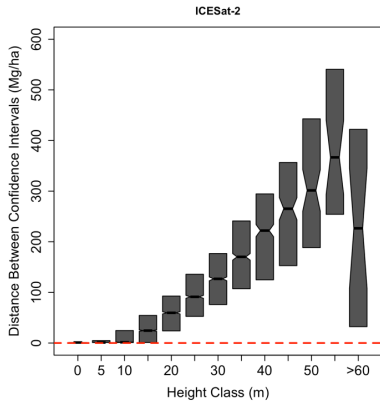
947 Yu, Y., Saatchi, S., 2016. Sensitivity of L-Band SAR Backscatter to Aboveground Biomass of  
948 Global Forests. *Remote Sens.* 8, 522. <https://doi.org/10.3390/rs8060522>

949 Zolkos, S.G., Goetz, S.J., Dubayah, R., 2013. A meta-analysis of terrestrial aboveground  
950 biomass estimation using lidar remote sensing. *Remote Sens. Environ.* 128, 289–298.  
951 <https://doi.org/10.1016/j.rse.2012.10.017>  
952 Zscheischler, J., Mahecha, M.D., Avitabile, V., Calle, L., Carvalhais, N., Ciais, P., Gans, F.,  
953 Gruber, N., Hartmann, J., Herold, M., 2017. Reviews and syntheses: An empirical  
954 spatiotemporal description of the global surface-atmosphere carbon fluxes: opportunities  
955 and data limitations. *Biogeosciences* 14, 3685–3703.  
956

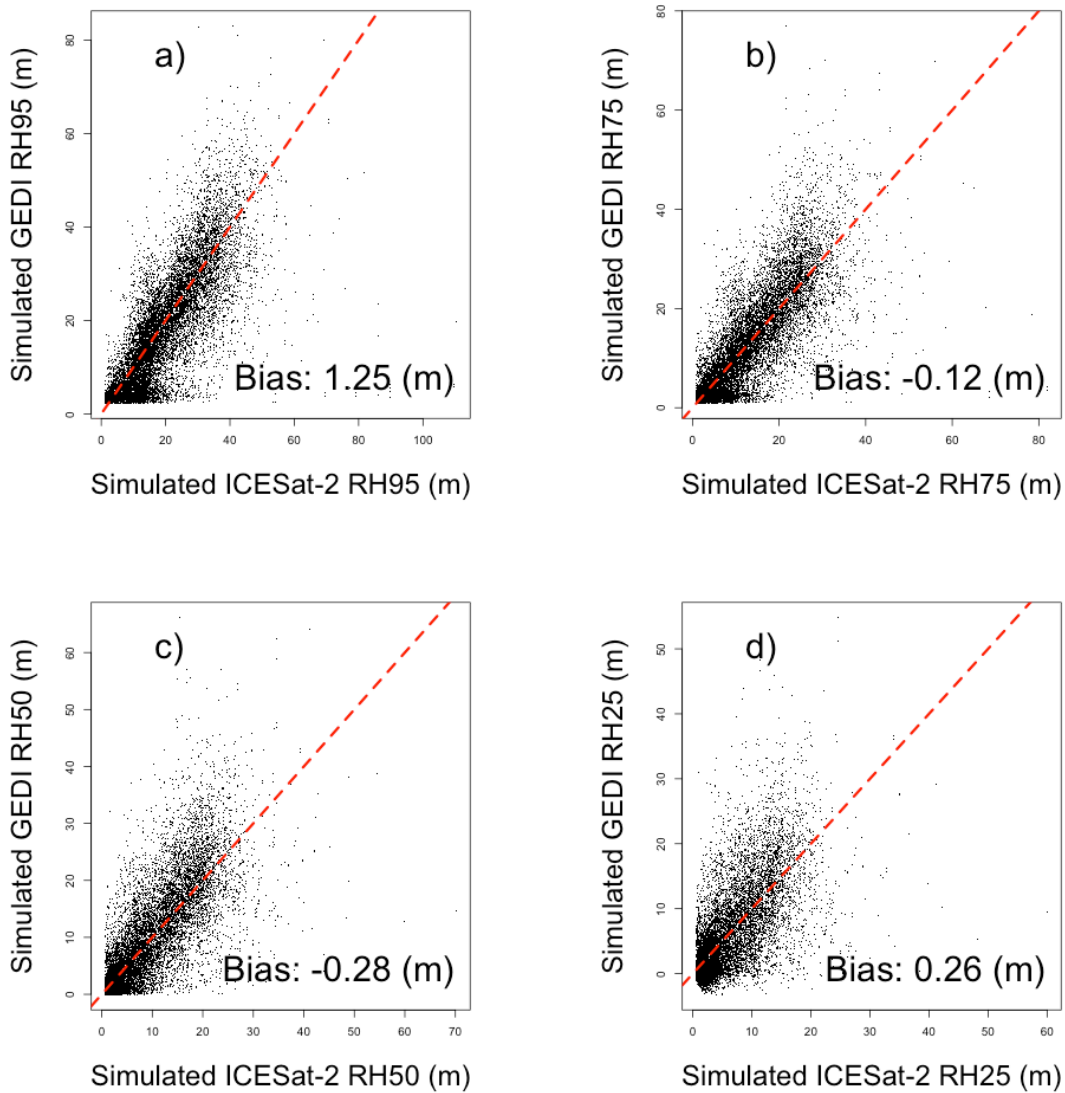


958

959 **SI Fig 1 Shows the model fit performance for the new ALS-based Sonoma County**  
960 **biomass algorithms. This was a square root transformed parametric model predicting**  
961 **field estimated biomass as a function of ALS %canopy cover, 50<sup>th</sup> percentile height and**  
962 **90<sup>th</sup> percentile height.**



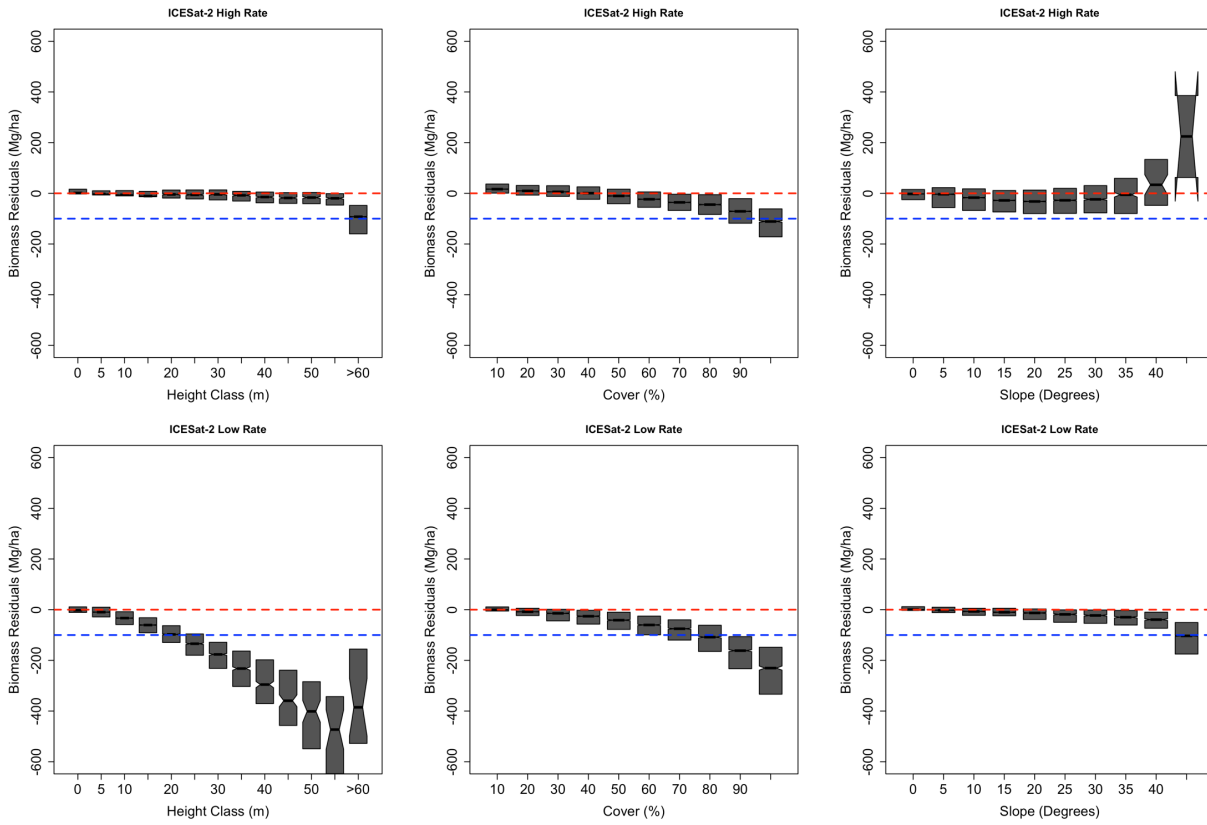
964 **SI Fig 2** The distance between the extents of reference and simulated mission confidence  
965 intervals is shown for ICESat-2 (a-c), NISAR (d-f), GEDI power beam (g-i), and GEDI  
966 coverage beam (j-l), plotted as a function of canopy height, % canopy cover, and slope.  
967 Larger values here represent greater deviations between the extents of the confidence  
968 intervals, indicating that either our reference data or (more likely) mission estimates of  
969 confidence intervals do not capture true uncertainties.



970

971 **SI Fig 3** comparison of ICESat-2 and GEDI height metrics for higher signal photon rate

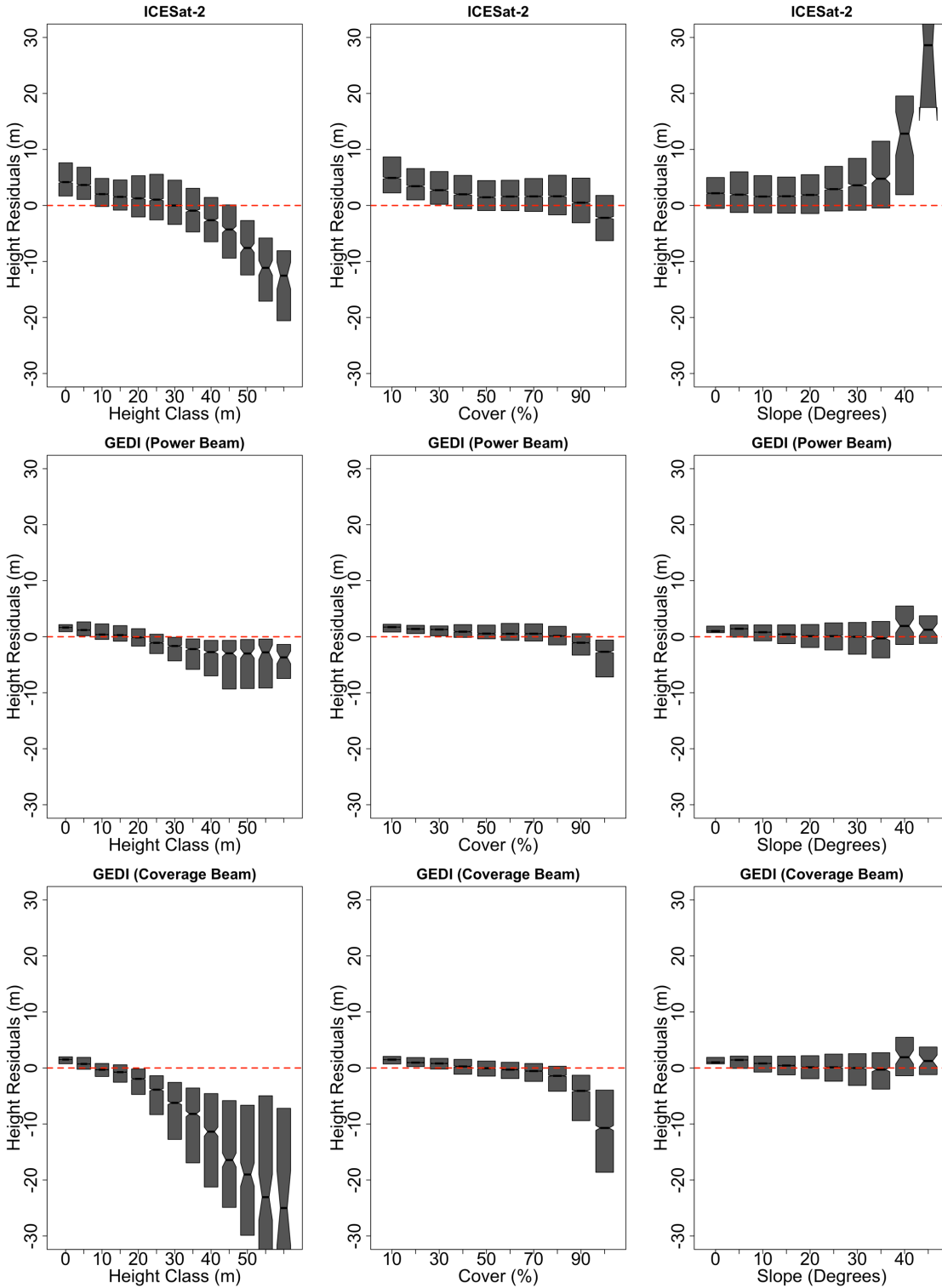
972



973

974 **SI Fig 4 A comparison of simulated high signal photon rate ICESat-2 estimates to low**  
975 **signal photon rates for biomass residuals compared to environmental gradients.**

976



977

978 SI Fig 5. Height residuals (RH98\_spaceborne – p98\_ALS) are plotted against forest height,

979 %canopy cover and slope.